Molecular Therapy
Nucleic Acids
Original Article

Exosomal Delivery of AntagomiRs Targeting Viral and Cellular MicroRNAs Synergistically Inhibits Cancer Angiogenesis

Jianguo Wang,[1,3,9] Qiang Jiang,[1,9] Oluwasijibomi Damola Faleti,[2,9] Chi-Man Tsang,[7,8,9] Min Zhao,[4] Gongfa Wu,[5] Sai-Wah Tsao,[7] Minyi Fu,[6] Yuxiang Chen,[1] Tengteng Ding,[1] Tuotuo Chong,[1] Yufei Long,[1] Xu Yang,[1] Yuanbin Zhang,[1] Yunxi Cai,[1] Hanzhao Li,[1] Manli Peng,[1] Xiaoming Lyu,[2,10] and Xin Li[1,10]

[1]Shenzhen Key Laboratory of Viral Oncology, The Clinical Innovation & Research Center (CIRC), Shenzhen Hospital, Southern Medical University, Shenzhen, China; [2]Departmrent of Laboratory Medicine, The Third Affiliated Hospital, Southern Medical University, Guangzhou, China; [3]Department of Radiation Oncology, The First Affiliated Hospital of USTC, Division of Life Sciences and Medicine, University of Science and Technology of China, Hefei, Anhui, 230001, China; [4]PANACRO (Hefei) Pharmaceutical Technology Co., Ltd., Hefei, China; [5]Department of Pathology, Zengcheng District People's Hospital of Guangzhou City, Guangzhou, China; [6]Otolaryngology-Head and Neck Surgery Department, Zhongshan City People's Hospital, Zhongshan, China; [7]School of Biomedical Sciences, Li Ka Shing Faculty of Medicine, University of Hong Kong, Hong Kong SAR, China; [8]Department of Anatomical and Cellular Pathology, State Key Laboratory of Translational Oncology, Faculty of Medicine, Chinese University of Hong Kong, Hong Kong SAR, China

Nasopharyngeal carcinoma (NPC) is an Epstein-Barr virus (EBV)-associated cancer characterized by a high degree of recurrence, angiogenesis, and metastasis. The importance of alternative pro-angiogenesis pathways including viral factors has emerged after decades of directly targeting various signaling components. Using NPC as a model, we identified an essential oncogenic pathway underlying angiogenesis regulation that involves the inhibition of a tumor suppressor, Spry3, and its downstream targets by EBV-miR-BART10-5p (BART10-5p) and hsa-miR-18a (miR-18a). Overexpression of EBV-miR-BART10-5p and hsa-miR-18a strongly promotes angiogenesis *in vitro* and *in vivo* by regulating the expression of VEGF and HIF1-α in a Spry3-dependent manner. *In vitro* or *in vivo* treatment with iRGD-tagged exosomes containing antagomiR-BART10-5p and antagomiR-18a preferentially suppressed the angiogenesis and growth of NPC. Our findings first highlight the role of EBV-miR-BART10-5p and oncogenic hsa-miR-18a in NPC angiogenesis and also shed new insights into the clinical intervention and therapeutic strategies for nasopharyngeal carcinoma and other virus-associated tumors.

INTRODUCTION

Persistent and asymptomatic virus infections play crucial roles in oncogenesis. Currently, about 15%–20% of human cancers are either casually associated or induced by oncogenic viral factors.[1] Viruses use a variety of tactics to drive oncogenesis and tumor progression, and one way is the regulation of angiogenesis. The formation of new and leaky vessels (angiogenesis) is regulated at multiple levels and contributes to poor cancer prognosis by promoting growth, invasion, and metastasis of cancer cells.[2,3] Virus-associated cancers such as Kaposi's sarcoma (herpesvirus),[4] cervical cancer (human papilloma virus),[5] nasopharyngeal carcinoma (NPC),[6] Burkitt lymphoma,[7] and gastric carcinoma[8] (Epstein-Barr virus [EBV]) also show high degrees of vascularization with the increased expression of multiple angiogenic factors such as basic fibroblast growth factor (bFGF) and vascular endothelial growth factor (VEGF). Consequently, anti-angiogenic therapy has been proposed as a therapeutic option for virus-associated cancers. As clinical needs remain unmet, it is crucial to develop novel antiangiogenesis therapeutics to complement the existing treatment options.

MicroRNAs (miRNAs) are essential gene regulators and function as tumor suppressors or oncogenes in cancer.[9,10] Extensive studies have revealed that microRNA dysregulation influences some critical pathways in cancer cells, including angiogenesis.[11,12] During angiogenesis, microRNAs function as regulators by modulating the activity of endothelial cells via non-cell-autonomous and cell-autonomous mechanisms.[13] Additionally, microRNAs can be transferred into endothelial cells by cancer-derived extracellular vesicles to regulate cancer angiogenesis.[14,15] These insights into the roles of microRNAs in cancer angiogenesis have made microRNAs attractive tools and targets for novel therapeutic approaches.

NPC, an infection-associated cancer, is strongly driven by EBV.[16,17] 25 viral microRNA precursors (3 BHRF1 pre-microRNAs and 22

Received 14 April 2020; accepted 14 August 2020;
https://doi.org/10.1016/j.omtn.2020.08.017.

[9]These authors contributed equally to this work.

[10]Senior author

Correspondence: Xiaoming Lyu, Department of Laboratory Medicine, The Third Affiliated Hospital, Southern Medical University, Guangzhou 510630, China.
E-mail: xiaomlyu@smu.edu.cn
Correspondence: Xin Li, Shenzhen Key Laboratory of Viral Oncology, The Clinical Innovation & Research Center (CIRC), Shenzhen Hospital, Southern Medical University, Shenzhen 518102, China.
E-mail: xinli268@gmail.com

BART pre-microRNAs) encoded by the virus form 48 mature microRNAs that regulate viral latency and cancer metabolism.[18–21] A prominent feature of NPC is angiogenesis, and patients usually have epistaxis.[22,23] To date, the first line of NPC treatment remains the combination of radiotherapy and chemotherapy. However, a bulk of patients experience disease progression despite the initial response to treatment.

Using NPC as a research model, in this study, we show for the first time the novel synergetic role of cellular and viral microRNAs in cancer angiogenesis. Our experiments identified miR-18a, a member of the oncogenic miR-17-92 cluster, and BART10-5p, a viral microRNA, as crucial regulators in NPC angiogenesis. This work is based on our previous studies, in which we performed an unbiased microRNA profiling analysis of NPC primary tissues.[24] The underlying molecular mechanism by which the two microRNAs promote cancer angiogenesis involves the harmonious downregulation of Spry3's expression (tumor suppressor) and, consequently, the activation of the Spry3/MEK/Erk-dependent pathways. Following the identification of two novel microRNAs as targets for antiangiogenesis therapy, we developed antagomiR-BART10-5p and antagomiR-18a enclosed in iRGD-tagged HUVEC (human umbilical vein endothelial cell)-derived exosomes to inhibit NPC angiogenesis. The engineered exosomes improved the anti-angiogenic and anti-tumor effects of the treatment and also was well-tolerated in animal studies. Our findings provide new insights into NPC angiogenesis regulation by microRNAs (viral and host) and highlight the potential of antagomiRs for use in cancer therapy.

RESULTS

EBV-miR-BART10-5p (BART10-5p) and hsa-miR-18a (miR-18a) Are Novel Targets for Antiangiogenesis Therapy in NPC

MicroRNAs are pivotal modulators in the development and progression of tumor angiogenesis.[10,11] To date, only a handful of microRNAs have been reported to participate in NPC angiogenesis. In this study, we screened for cellular and EBV-encoded microRNAs that were associated with NPC angiogenesis. First, we detected the microvessel density (MVD) in 20 NPC tissues and found relatively higher expressions of CD31, CD34, and VEGFR1 (Figure 1A; Figures S1A, S1C, and S1I) compared with NP (Figure 1A; Figures S1B, S1D, and S1J), demonstrating an ongoing angiogenic process in NPC tissues.

We previously performed microRNA expression profiling using microarrays and identified 69 differentially expressed microRNAs in NPC and non-cancerous NP tissues. Seven EBV-encoded microRNAs (EBV-miR-BART10, BART7, BART3, BART1, BART8, BART9, and BART5) were top-ranked.[24] Accordingly, we applied qPCR analysis to confirm the expression of EBV-miR-BART10 in HONE1-EBV cells and 20 NPC tissues (Figure 1D). High expression of miR-18a in NPC tissues compared to NP tissues was also verified (Figure 1C). Furthermore, western blot and enzyme-linked immunosorbent assay (ELISA) revealed a relatively high expression of VEGF after overexpression of EBV-miR-BART10 and miR-18a compared with other microRNAs (Figures 1B and 1E), suggesting a strong correlation between NPC angiogenesis and the expression levels of EBV-miR-BART10 and miR-18a. Thus, these two microRNAs were selected for subsequent experiments *in vitro* and *in vivo*.

Previous studies have shown that the 3p and 5p of microRNA have different biological activity. To choose EBV-miR-BART10-3p (BART10-3p) or BART10-5p, we performed HUVEC tube formation and chicken chorioallantoic membrane (CAM) assays. HUVECs are capable of forming tube structures while mammalian placenta has some marked similarities with the chick yolk sac and CAM assays in gas and nutrition exchange functions. Our data showed that BART10-5p possessed a higher tube formation-promoting effect than that of BART10-3p in HUVECs and CAM assays (Figure S2A). Conversely, the downregulation of BART10-5p showed a superior angiogenesis-inhibiting effect in NPC cells compared with BART10-3p in both tube formation and CAM assays (Figure S2B). Therefore, we selected BART10-5p for the subsequent experiments.

To further verify the role of BART10-5p and miR-18a, we selected an EBV-negative NPC cell line and two EBV-positive cell lines as *in vitro* models: HONE1 cells have a relatively low endogenous expression of miR-18a (Figure S3A), whereas HONE1-EBV and C666-1 cells have high endogenous expression of BART10-5p and miR-18a (Figures S3A and S3B). In accordance with previous results, BART10-5p and miR-18a were able to promote NPC angiogenesis in *in vitro* models. Strikingly, co-treatment with mimics or agomiRs of BART10-5p and miR-18a got a stronger response, suggesting that BART10-5p and miR-18a have a synergistic effect on angiogenesis (Figures 2A–2D). Conversely, we treated HONE1-EBV and C666-1 NPC cells with inhibitors or antagomiRs of BART10-5p and miR-18a respectively or simultaneously. We observed a varying degree of inhibitory effects on NPC angiogenesis, and, also, co-treatment gave a stronger inhibitory effect (Figures 2E–2H; Figure S4). Thus, these results suggest that BART10-5p and miR-18a are closely associated with NPC angiogenesis and may act as novel targets for antiangiogenesis therapy.

BART10-5p and miR-18a Directly Co-target Spry3 and Co-influence Spry3-Associated Pathways

Next, we switched our attention to the potential targets of BART10-5p and miR-18a. We first searched candidate targets using two online bioinformatics tools (BiBiserv2 and RNAhybrid). Notably, of all candidates, Spry3 was exclusively predicted as a target gene co-regulated by BART10-5p and miR-18a (Figure 3A). Although two microRNAs targeted the same gene, they bound different sites in the 3′ UTR region of Spry3 (Figure 3A). Furthermore, we found that endogenous expression of Spry3 in 20 NPC tissues was significantly low compared with 20 NP tissues (Figure S5A), suggesting that Spry3 may have a tumor-suppressor function in NPC. Overexpression of BART10-5p and miR-18a downregulated the Spry3 protein expression level in HONE1 cells (Figure 3D). Conversely, downregulation of BART10-5p and miR-18a elevated the Spry3 protein expression levels in HONE1-EBV and C666-1 cells (Figure 3E; Figure S5D). After

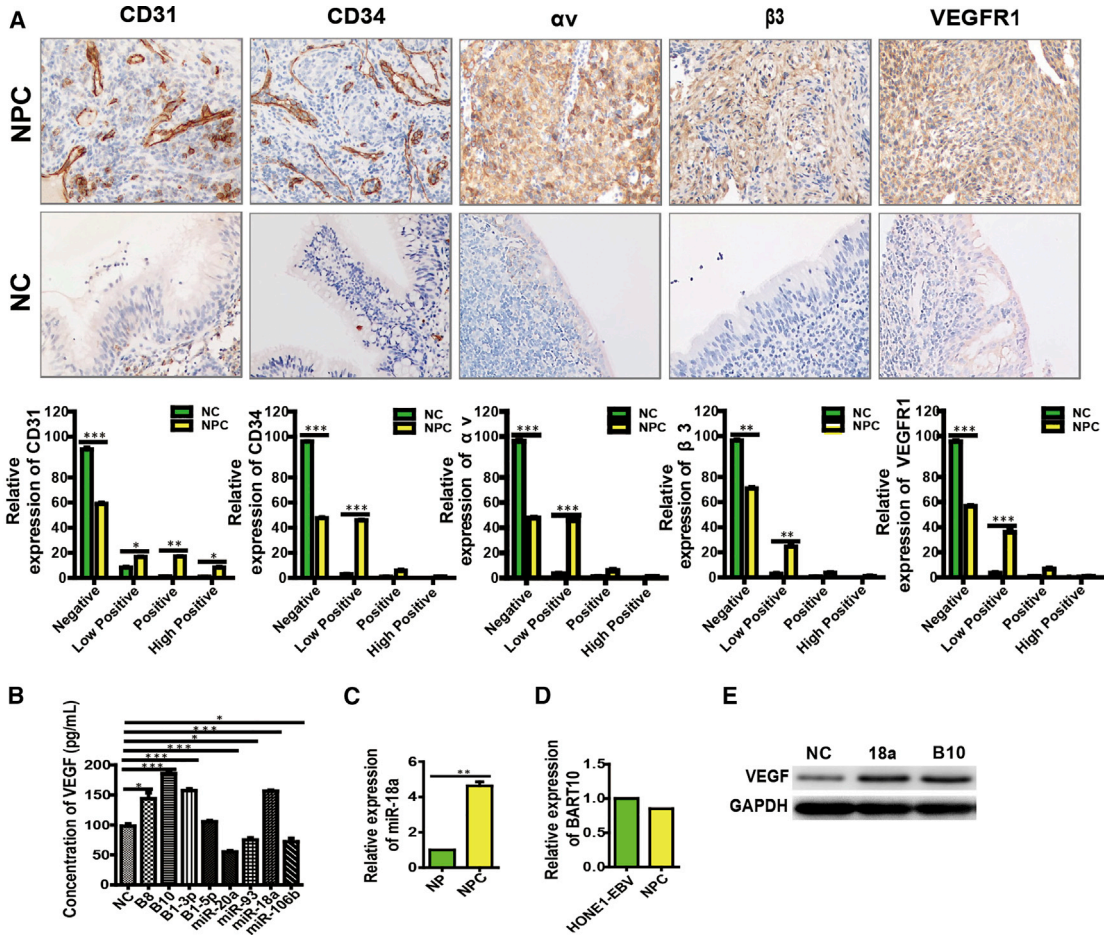

Figure 1. The Stronger Correlation of the Expression Levels of BART10 and miR-18a with NPC Angiogenesis

(A) The expression of CD31, CD34, αv, β3, and VEGFR1 in NPC and NP. All images were taken at ×200 original magnification. HPF, high-power field. (C) The endogenous expression of miR-18a in NP and NPC tissues, (D) The endogenous expression of BART10 in NPC tissue and NPC cell.The stronger correlation of the expression levels of BART10 and miR-18a with VEGF presented in ELISA assay (B) and western blot assay (E).

performing small interfering RNA (siRNA) knockdown of Spry3, we observed that VEGF expression was accordingly upregulated (Figure 3F; Figure S5C). Tube formation and CAM assays revealed that Spry3 was also closely linked with angiogenesis in NPC (Figures S6A and S6B).

To confirm the direct regulation of Spry3 by BART10-5p and miR-18a, we conducted luciferase reporter assays. The luciferase activity of the wild-type (WT) 3′ UTR of Spry3 but not the mutant 3′ UTR was significantly reduced by miR-18a mimics (Figure 3C). Similarly, the co-transfection of BART10-5p mimics significantly decreased luciferase reporter activity (Figure 3B). Collectively, these results demonstrated that BART10-5p and miR-18a suppressed Spry3 gene by directly binding to its 3′ UTR region.

To delineate the regulatory mechanism of Spry3 by BART10-5p and miR-18a, we examined the major components of Spry3-dependent or associated pathways in NPC. After transfecting agomiR-BART10-5p and agomiR-18a respectively or co-transfecting two agomiRs in HONE1 cells, we noticed that agomiR-BART10-5p and agomiR-18a upregulated the protein expression levels of Ras, c-Raf, MEK1/2, mTOR, eIF4E1, Erk1/2, HIF1-α, mmp2, and VEGF. The co-transfection of two agomiRs gave a stronger response compare to the single microRNA agomiR (Figure 3D). Consistently, the transfection of antagomiR-BART10-5p, antagomiR-18a, or co-treatment of two antagomiRs downregulated the expression of Ras, c-Raf, MEK1/2, mTOR, eIF4E1, Erk1/2, HIF1-α, mmp2, and VEGF in HONE1-EBV and C666-1 cells (Figure 3E; Figure S5D).

To further verify whether BART10-5p and miR-18a regulated Spry3 and its associated pathway, we performed several recovery assays. Western blot assay showed that protein levels of Ras, c-Raf, MEK1/2, mTOR, eIF4E1, Erk1/2, HIF1-α, mmp2, and VEGF were modestly downregulated after co-transfecting agomiR-18a and Spry3 plasmid

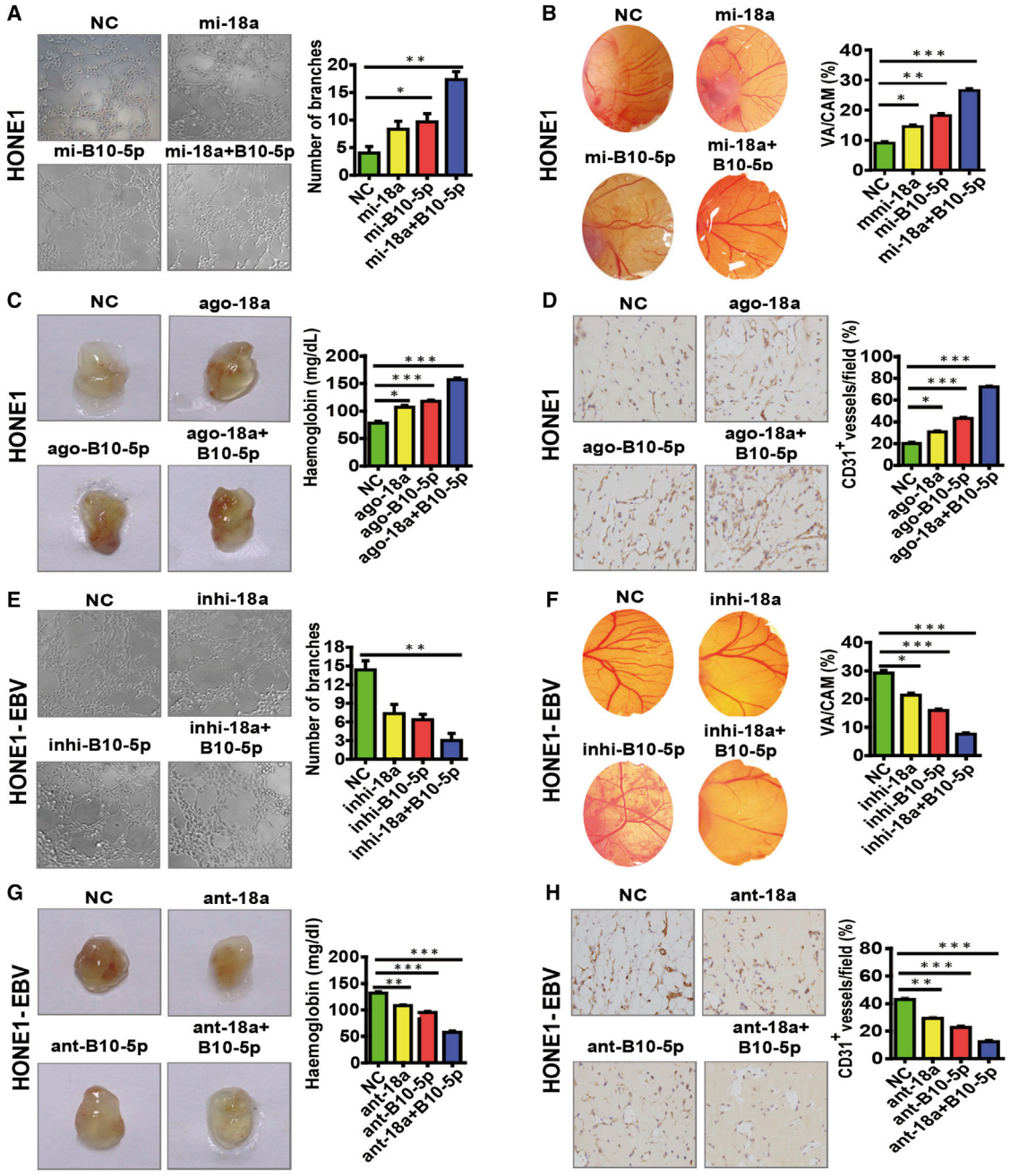

Figure 2. EBV-miR-BART10-5p and hsa-miR-18a Have a Crucial Role in NPC Angiogenesis

(A–C) BART10-5p and miR-18a were able to promote NPC angiogenesis individually in *in vitro* models (tube formation assay and CAM assay) (A and B) and in an *in vivo* model (Matrigel plug assay) (C). (E–G) Inhibition of BART10-5p and miR-18a were able to inhibit NPC angiogenesis individually in *in vitro* models (tube formation assay and CAM assay) (E and F) and in an *in vivo* model (Matrigel plug assay) (G). Furthermore, co-treatment with mimics/agomiRs inhibitor or antagomiRs of BART10-5p and miR-18a got a stronger response. Furthermore, co-treatment with BART10-5p and miR-18a got a stronger response. (C and G) Representative images (left) and hemoglobin quantification (right) of the Matrigel plug assay (n = 3, Student's t test). (D and H) Expression of CD31, which represents MVD in Matrigel plug sections (n = 3, Student's t test). Original magnification, ×200. All images were taken at ×200 original magnification. All bars and error bars stand for mean values and corresponding SEM. *$p < 0.05$, **$p < 0.01$, ***$p < 0.001$.

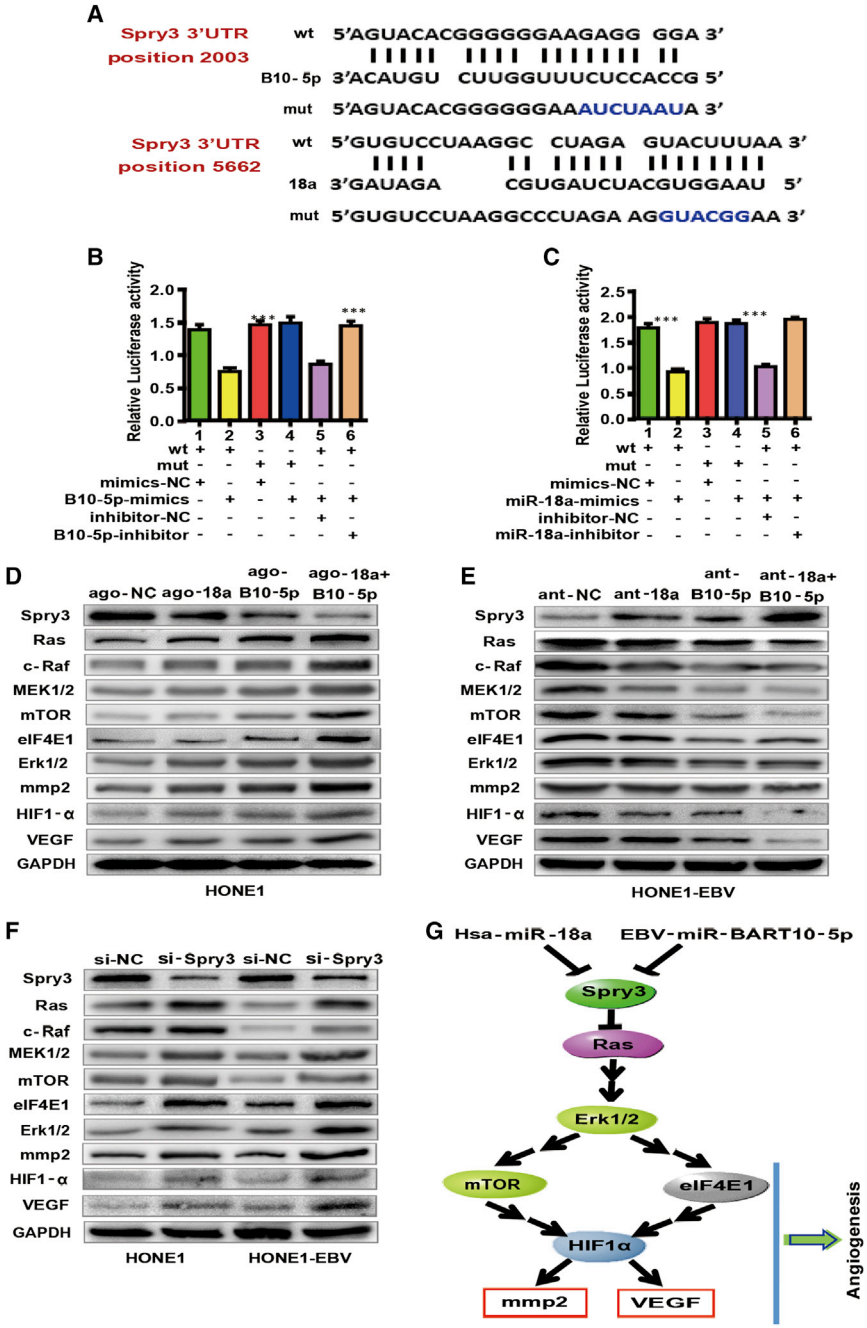

Figure 3. EBV-miR-BART10-5p and hsa-miR-18a directly Co-target Spry3 and Co-influence Spry3-Dependent Pathways

(A) Computational analysis of BART10-5p and/or miR-18a and its putative binding sequences in the 3′ UTR of Spry3. A mutation was obtained in the complementary site that bound to the seed region of BART10-5p or miR-18a. BART10-5p (B) and miR-18a (C) directly targeted the Spry3 3′ UTR. One-way ANOVA and Dunnett's multiple comparison test. Mean ± SEM. ***$p < 0.001$. The expression levels of Spry3, MEK1/2, Erk1/2, HIF1-α, and VEGF in HONE1 cells after upregulation/downregulation of BART10-5p and/or miR-18a expression with agomiRs (D)/antagomiRs (E). GAPDH was used as a loading control. (F) Effect of Spry3 silencing on the expression levels of MEK1/2, Erk1/2, HIF1-α, and VEGF in HONE1 and HONE1-EBV cells. (G) Schematic representation of mechanisms by which BART10-5p and miR-18a mediate angiogenic function in NPC.

(Figure S5B, left), or agomiR-BART10-5p and Spry3 plasmid (Figure S5B, middle), compared to negative control and agomiR-18a or agomiR-BART10-5p. Notably, co-transfection of agomiR-BART10-5p or agomiR-18a and Spry3 plasmid was found to significantly recover the expression levels of Ras, c-Raf, MEK1/2, mTOR, eIF4E1, Erk1/2, HIF1-α, mmp2, and VEGF compared to negative control and agomiR-18a combined agomiR-BART10-5p (Figure S5B, right). In sum, these results indicated that BART10-5p and miR-18a influenced NPC angiogenesis by regulating Spry3 and its downstream pathways associated with angiogenesis.

The Enhanced Targeting Ability of iRGD-exo *In Vitro* and *In Vivo*

To validate whether iRGD-exo can well bind to αvβ3 integrin-positive NPC cells, HONE1 and HONE1-EBV cells, which profoundly expresses αvβ3 integrin subunits on its surface, were incubated with iRGD-exo or blank-exo labeled with 1,1′-dioctadecyl-3,3,3′,3′-tetramethylindocarbocyanine perchlorate (DiI). (Isolation and identification of iRGD-tagged exosomes are shown in Supplemental Information.) The results demonstrated that the iRGD peptide significantly enhanced the binding ability of exosomes to target cells (Figure 4A). To evaluate the biodistribution of iRGD-exo compared with blank-exo *in vivo*, we labeled them with near-infrared dye DiD (1,1′-dioctadecyl-3,3,3′,3′-tetramethylindodicarbocyanine perchlorate) and injected the HONE1-EBV tumor-bearing animal models through a tail vein. Mice were sacrificed 24 h after systemic administration. The fluorescence intensities in a tumor and other major organs (heart, spleen, kidney, lung, and liver) were quantified. Results demonstrated that, as compared to iRGD-exo-DiD, the blank-exo-DiD primarily accumulated in the liver, the lungs, and the spleen. Additionally, a low fluorescent signal was detected in a tumor (Figure 4B). In contrast to blank-exo-DiD, iRGD-exo-DiD administration significantly enhanced the fluorescence intensity in the tumor (Figure 4B). Of note, the engineered exosomes were well tolerated by the animals, and no noticeable damage was observed in vital

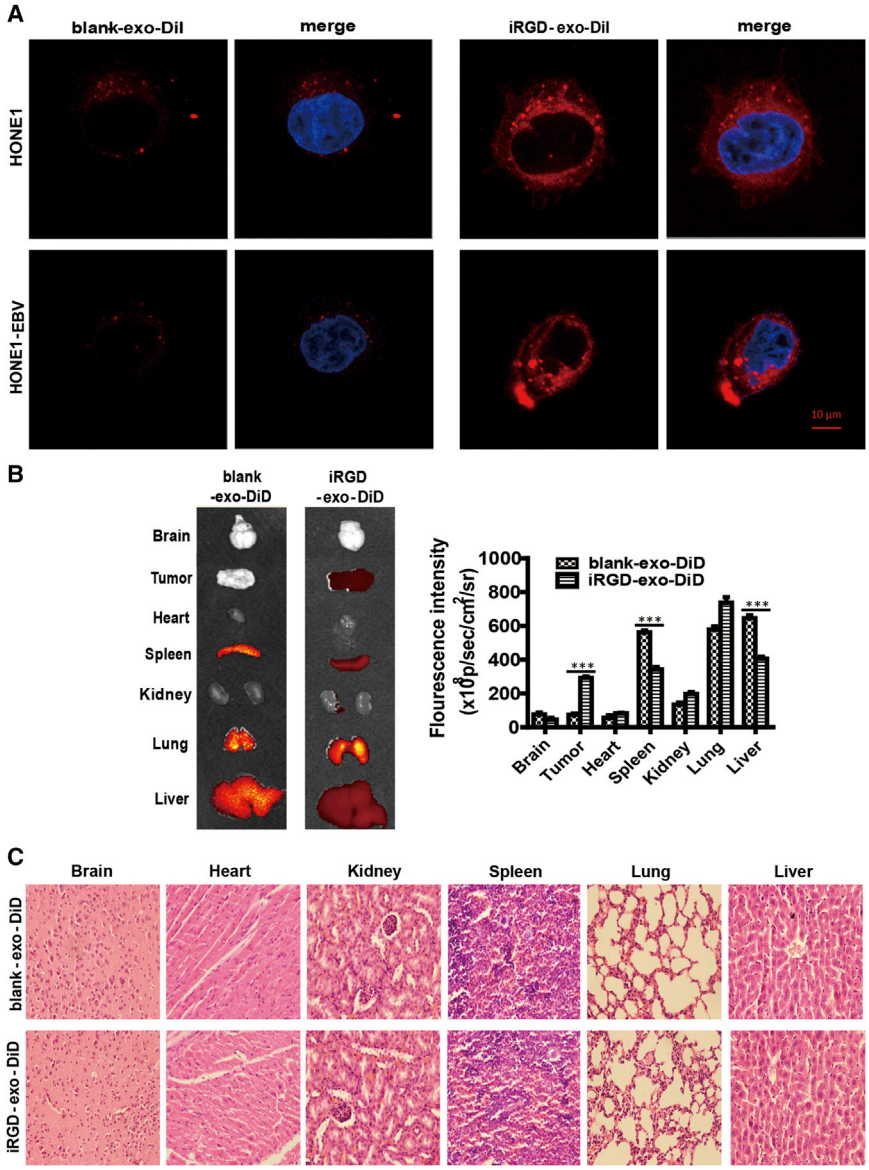

Figure 4. Binding of iRGD-exo to NPC Cell Lines *In Vitro* and Targeting of iRGD-exo *In Vivo*

(A) Exosomes and the targeting ability that localized the cell membrane and cytoplasm of HONE1 or HONE1-EBV cells with confocal microscopy images. Original magnification, ×630; scale bar, 10 μm. (B) *Ex vivo* fluorescence imaging of various major organs from nude mice bearing HONE1-EBV tumors. The sequence of organs from top to bottom is as follows: brain, tumor, heart, spleen, kidney, lung, liver. Results are mean ± SD, n = 5. (C) Various organs from mice treated as described in (B) were detected with hematoxylin and eosin (H&E) staining.

body organs (Figure 4C). These findings indicated that iRGD-exo presented excellent targeting ability and biological security in NPC *in vivo*.

Antiangiogenesis Efficacy of iRGD-exo-AntagomiRs *In Vitro* and *In Vivo*

Before assessing the efficacy of iRGD-exo-antagomiRs as an antiangiogenesis therapy of NPC, we investigated the expression of an angiogenesis-associated regulatory factor in 20 NPC tissues. Abundant expression of CD31 and CD34 was detected in NPC tissues (Figure 1A; Figures S1A and S1C), which demonstrated the angiogenic process in NPC tissues. We then assessed the antiangiogenesis capacity of iRGD-exo-antagomiRs regarding NPC *in vitro* and *in vivo*. Taking advantage of tube formation assay, Matrigel plug assay, and CAM assay, we found that iRGD-exo-antagomiR-BART10-5p and iRGD-exo-antagomiR-18a treatment decreased the tube formation of HUVECs and angiogenesis formation in the Matrigel plug assay and CAM model. Of note, co-treatment with iRGD-exo-antagomiR-BART10-5p and iRGD-exo-antagomiR-18a synergistically inhibited angiogenesis in three experiments (Figures 5A–5D).

Given the antiangiogenesis effect shown by iRGD-exo-antagomiR-BART10-5p and iRGD-exo-antagomiR-18a *in vitro* and *in vivo*, we further explored their therapeutic effects using the NPC animal model. First, we established nude mice bearing subcutaneously implanted tumor cells (HONE1-EBV cells). Afterward, they were randomly divided into seven groups and the groups were treated as follows: (1) free exosomes, as a control; (2) exo-antagomiR-18a; (3) exo-antagomiR-BART10-5p; (4) exo-antagomiR-18a and exo-antagomiR-BART10-5p; (5) iRGD-exo-antagomiR-18a; (6) iRGD-exo-antagomiR-BART10-5p; and (7) iRGD-exo-antagomiR-18a and iRGD-exo-antagomiR-BART10-5p. After 16 days of treatment, a remarkable inhibition of tumor growth was observed in the animals treated with iRGD-exo-antagomiRs compared with exo-antagomiRs (Figures 6A–6D). Also, compared to a single treatment with either of the exo-antagomiRs, co-treatment showed a greater inhibitory effect. This result was consistent with the three previous experiments. This growth inhibition was further confirmed by carrying out immunohistochemical staining for CD31, the frequently used angiogenesis marker for MVD. We observed relatively lower expression of CD31 in tumors treated with the iRGD-exo-antagomiRs groups than either free exosome control or the exo-antagomiRs groups (Figure 6E). We also noticed significant downregulation of regulating factors, namely VEGF, mmp2, HIF1-α, and Erk1/2, which are downstream of Spry3 in the iRGD-exo-antagomiRs groups compared to the free exosome control or exo-antagomiRs groups (Figure S8). Furthermore, we assessed the

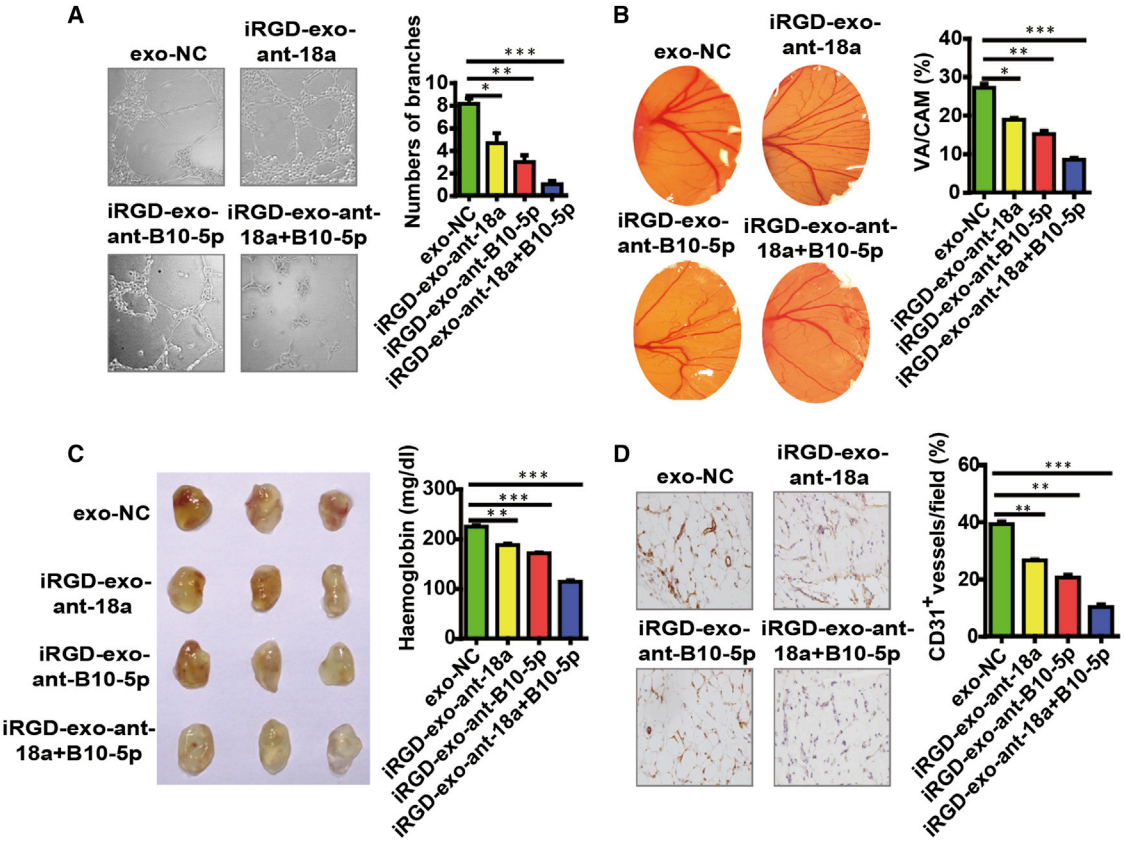

Figure 5. *In Vitro* and *In Vivo* Antiangiogenesis Efficacy of iRGD-exo-AntagomiRs

Antiangiogenesis efficacy of iRGD-exo-antagomiRs *in vitro,* (A) tube formation assay and (B) CAM assay) (n = 5, Student's t test). HPF; original magnification, ×200. All bars and error bars stand for mean values and the corresponding SEM. *p < 0.05, **p < 0.01, ***p < 0.001). (C) Antiangiogenesis efficacy of iRGD-exo-antagomiRs *in vivo* (Matrigel plug assay). Images (left) and haemoglobin quantification (right) (n = 3, Student's t test). (D) The expression of CD31, which represents MVD in Matrigel plug sections (n = 5, Student's t test). Original magnification, ×200.

level of tissue damage following repeated systemic intravenous administration of iRGD-exo-antagomiRs and conducted histological analysis. Notably, our histological analysis showed no tissue damage or any other abnormalities in several major body organs (Figure 6F).

DISCUSSION

Our study describes a novel oncogenic pathway underlying angiogenesis regulation that involves BART10-5p and miR-18a inhibiting tumor suppressor Spry3 and its downstream targets. These findings establish a synergistic role between virus and host microRNAs in the regulation of angiogenesis of virus-associated cancer. The formation of new and leaky blood vessels supports uncontrolled growth, infiltration, and metastasis and thereby contributes to tumor recurrence and short survival. In the past decades, various US Food and Drug Administration (FDA)-approved antiangiogenesis drugs have emerged. However, clinical outcomes are unsatisfactory due to the emergence of alternative angiogenesis factors, inefficient drug delivery, and unsatisfactory safety profile.[2] Thus, we developed iRGD-exo-antagomiR-BART10-5p and iRGD-exo-antagomiR-18a, which specifically and efficiently inhibit tumor growth *in vivo*, thus highlighting their potential therapeutic application in the treatment of cancer. The host miR-17-92 cluster has been identified as an oncogenic microRNA cluster that is involved in the angiogenesis of several cancers.[25,26] A previous report showed that expression of miR-18a, a member of the oncogenic miR-17-92 cluster, is upregulated in the NPC samples and cell lines.[27] An increased level of miR-18a was found to correlate with EBV infection, lymph node metastasis, and low survival rate of NPC patients.[28] Recent evidence also suggests that viral microRNAs participate in metabolism,[19] metastasis,[29] and immune escape and are biomarkers of NPC.[30,31] We and others have shown that EBV-miR-BART7-3p and BART10-3p promoted EMT and metastasis in NPC by targeting tumor suppressor PTEN[18] and BTRC.[32]

To verify the role of host oncogenic microRNA and EBV-miR-BART on NPC angiogenesis, we analyzed the expression of some human oncogenic and BART microRNAs in NPC samples and found significant upregulation of BART10-5p and miR-18a expression. To rule out the effect of background angiogenic factors, we established NPC cell lines that have a low angiogenesis level and a low level of

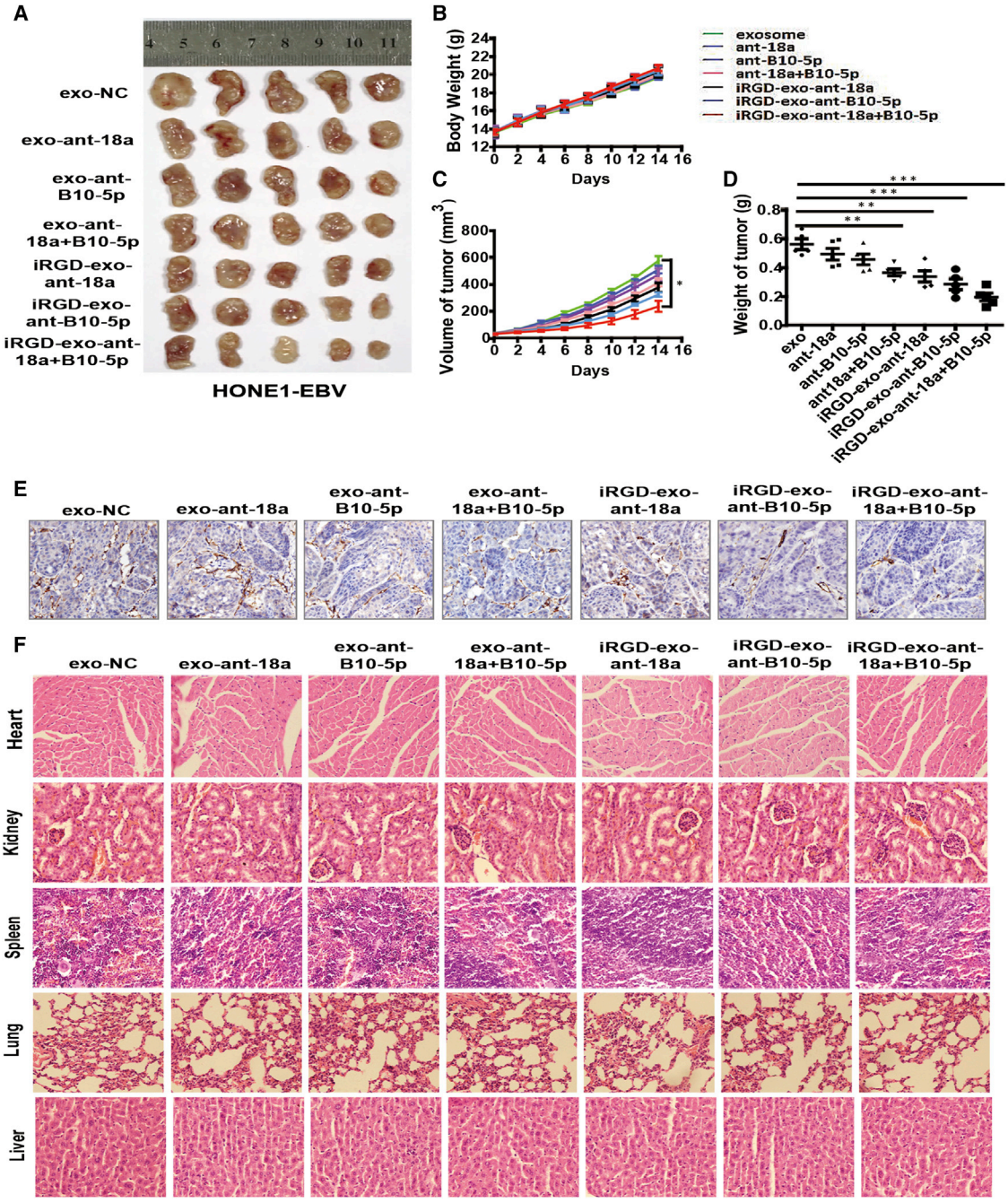

Figure 6. Antiangiogenesis Therapeutic Effects of iRGD-exo-AntagomiRs in Xenograft Mouse Models of NPC

(A) Excised tumors collected from each group. (B–D) Body weights (B), tumor volume (C) and weights of tumor (D) were calculated for each group. All bars and error bars stand for mean values and the corresponding SEM. *$p < 0.05$, **$p < 0.01$, ***$p < 0.001$). (E) The expression of CD31, which represents MVD in tumor sections of HONE1-EBV xenografts of tumor. Original magnification, ×200. (F) H&E staining of major organs following antiangiogenesis therapy of iRGD-exo-antagomiRs in NPC xenograft mouse models (n = 5).

BART10-5p and miR-18a expression. Using different assays, we showed that BART10-5p and miR-18a could propel angiogenesis in these selected NPC cell lines. Interestingly, co-treatment of either BART10-5p and miR-18a can synergistically promote angiogenesis. Our data not only highlight the role of cellular and viral microRNA in NPC angiogenesis, but they also show the importance of Spry3 in the regulation of tumor angiogenesis. Nachmani et al.[33] also showed that human cytomegalovirus (HCMV), another herpesvirus,

escaped immune system elimination via its miR-UL112, which acts synergistically with a host miR-376a.

The Sprouty family, which is composed of four members, including Spry1, Spry2, Spry3, and Spry4, was initially discovered in *Drosophila*.[34,35] The Sprouty family members are ligand-inducible negative regulators of the receptor tyrosine kinase (RTK), and their mechanism of action depends on the cell type and nature of the initiating growth factor.[36,37] Spry2 can block the activation of the Erk/MAPK pathway by the pro-angiogenic factor bFGF.[38] It also functions also as a tumor suppressor in breast, prostate, and liver cancer. Spry2 and Spry4 have been implicated in the cell proliferation and migration of osteosarcoma cells and endothelial cells.[39–41] However, there is no known report of Spry3's function in tumorigenesis. This study identified and verified that BART10-5p and miR-18a co-targeted Spry3 at different binding sites (Figure 3A). Our luciferase reporter assay supported the bioinformatics analysis that BART10-5p and miR-18a targeted Spry3 (Figures 3B and 3C). These observations explain why BART10-5p and miR-18a treatment exerted a synergistic effect on angiogenesis. Also, we found that the binding of BART10-5p and miR-18a to their co-target, Spry3, induced NPC angiogenesis by upregulating the expression of MEK1/2, Erk1/2, HIF1-α, and VEGF (Figures 3D–3G). Interestingly, inhibition/knockdown of Spry3 also increased the expression of VEGF (Figure 3F; Figure S5C). Similarly, Jones et al. also reported an inverse relationship between the levels of Spry1 mRNA and FGF2 mRNA.[39] Spry3 is a well-positioned regulator of the RKT mediated angiogenesis. Given the ability of BART10-5p and miR-18a to co-target Spry3, we developed antagomiRs to these microRNAs. Our antagomiRs showed a remarkable antiangiogenesis activity.

Exosomes (bio-derived nanoparticles) have enormous potential for drug delivery *in vivo*.[42–45] To improve its tumor targeting capability, we fused Lamp2b with iRGD, a targeting peptide for αv integrin. Lamp2b is an essential and well-characterized exosomal membrane protein.[46] The constructed exosome exhibited high specificity for the cancerous cells. This engineered exosome, which was first reported by Tian et al.,[47] has been shown to be biologically safe in other studies. Following repeated systemic intravenous administration of the iRGD-exo-antagomiRs, we conducted the histological analysis. Our data showed that no tissue damage or other abnormalities in several major body organs (Figure 6F). Overall, the constructed exosome provided specific tumor targeting in a mouse model (Figure 4B). Moreover, importantly, the iRGD-exo-antagomiRs showed significant anti-angiogenesis and anti-tumor therapeutic effects compared with non-targeting exosomes *in vivo* (Figure 6).

MATERIALS AND METHODS

Cell Culture

EBV-negative NPC cell line HONE1 and HEK293T cell were provided by the Cancer Research Institute Southern Medical University (Guangzhou, China). EBV-positive NPC cell line HONE1-EBV and C666-1 were obtained from Professor S.-W. Tsao, University of Hong Kong. HUVEC were kindly provided by Dr. Jihui Wang (Zhujiang Hospital of Southern Medical University, Guangzhou, China). All of NPC cell lines were cultured in RPMI-1640 (Corning, NY, USA) supplemented with 10% fetal bovine serum (FBS) (Bioind, Israel), 100 units/mL penicillin/streptomycin, while HEK293T cells and HUVEC grew in Dulbecco's modified Eagle's medium (DMEM, Corning, NY, USA) containing 10% FBS (Bioind, Israel) and 100 U/mL penicillin/streptomycin. All cells were maintained in a humid environment containing 5% CO_2 at 37°C. All of the cells were authenticated using short tandem repeat profiling, tested for Mycoplasma contamination.

Patients and Clinical Tissue Specimens

Twenty fresh primary NPC samples (no treatment before biopsy taking) and twenty fresh non-cancerous NP samples were collected from the People's Hospital of Zhongshan City, Guangdong, China. All fresh samples were immediately preserved in liquid nitrogen. Informed written consent was acquired from all subjects, and approval was received from the Ethics Committee of Zhongshan People's Hospital for the use of clinical materials for research purposes. The above 20 NPC and 20 NP specimens were used for immunohistochemical analysis and the endogenous expression analysis of Spry3 and EBV-miR-BART10.

ELISA

After transfection of mimics-BART8, mimics-BART10, mimics-BART1-3p, mimics-BART1-5p, mimics-miR-18a, mimics-miR-20a, mimics-miR-93, and mimics-miR-106b (transfection concentration, 50 nmol/L) into HONE1 cells, the amount of VEGF in cell-free supernatants was measured by a human VEGF ELISA kit (Neobio-science, Shenzhen, China) according to the manufacturer's instructions. The sequences of microRNAs are as follows: miR-18a mimics/agomir, sense, 5′-UAAGGUGCAUCUAGUGCAGAUAG-3′, antisense, 5′-AUCUGCACUAGAUGCACCUUAUU-3′; miR-18a inhibitor/antagomiR, 5′-CUAUCUGCACUAGAUGCACCUUA-3′; BART10-5p mimics/agomiR, sense, 5′-GCCACCUCUUUGGUUCUGUACA-3′, antisense, 5′-UACAGAACCAAAGAGGUGGCUU-3′; BART10-5p inhibitor/antagomiR, 5′-UGUACAGAACCAAAGAGGUGGC-3′; mimics/agomiR negative control, sense, 5′-UUCUCCGAACGUGUCACGUTT-3′, antisense, 5′-ACGUGACACGUUCGGAGAATT-3′; inhibitor/antagomiR negative control, 5′-CAGUACUUUUGUGUAGUACAA-3′; EBV-miR-BART1-3p mimics, 5′-UAGCACCGCUAUCCACUAUGUC-3′; EBV-miR-BART1-5p mimics, 5′-UCUUAGUGGAAGUGACGUGCUGUG-3′; hsa-miR-106b mimics: 5′-UAAAGUGCUGACAGUGCAGAU-3′; hsa-miR-93 mimics, 5′-CAAAGTGCTGTTCGTGCAGGTAG-3′; hsa-miR-20a mimics, 5′-TAAAGTGCTTATAGTGCAGGTAG-3′; EBV-miR-BART8, 5′-TACGGTTTCCTAGATTGTACAG-3′; EBV-miR-BART10, 5′-GCCACCUCUUUGGUUCUGUACA-3′. Briefly, 100 μL of cell-free supernatants was pipetted into each ELISA plate well, which was pre-coated with anti-human VEGF polyclonal antibody. After 1–2 h of incubation at 36°C, the plate was washed and then 100 μL of human VEGF conjugate was added to each well. Afterward, the plate was incubated at 36°C for 1–2 h, and excess detection antibody was removed. Subsequently, 100 μL of substrate solution was added to each well, and

the plate was incubated at 36°C shielded from the light to obtain color development. 30 min later, 100 μL of stop solutions were pipetted into each well. The absorbance of each well was measured with the use of a microplate reader (R&D Systems, Minneapolis, MN, USA) at 450 nm.

qRT-PCR

Total RNA was extracted from tissues or cells with RNAiso plus (Invitrogen, USA), and complementary DNA (cDNA) was synthesized with the PrimeScript RT reagent kit (Takara, China). The qRT-PCR assay was done in triplicate using SYBR Premix Ex Taq (Takara, China). The specific sense primers in this article are listed as follows: GAPDH, forward, 5′-CATGGGTGTGAACCATGAGA-3′, reverse, 5′-GTCTTCTGGGTGGCAGTGAT-3′; U6 forward, 5′-GGAACGATACAGAGAAGATTAGC-3′, reverse, 5′-TGGAACGCTTCACGAATTTGCG-3′; iRGD, forward, 5′-GGTGATAAAGGTCCAGATT-3′, reverse, 5′-GTTGTAGGAAAGCACGATG-3′; Spry3, forward, 5′-TGCTGCGGTGACAGATGATTT-3′, reverse, 5′-GTAGGCATGGTAGCCAGAGAC-3′; VEGF, forward, 5′-TCTACCTCCACCATGCCAAGT-3′, reverse, 5′-GATGATTCTGCCCTCCTCCTT-3′. For quantification of EBV-miR-BART10 and mature microRNAs, reverse transcription was performed using Takara microRNA assays (China). qRT-PCR was performed with an all-in-one microRNA qRT-PCR detection kit according to the manufacturer's protocol (GeneCopoeia, USA). U6 and GAPDH genes were used as microRNA and gene internal controls, respectively. The fold changes were calculated using the $2^{-\Delta\Delta Ct}$ method.

Plasmid Preparation and Cell Transfection

The expression vector GV141 (https://www.genechem.com.cn) containing the whole coding sequence of Lamp2 (iRGD + GenBank: NM_013995) was purchased from Genechem Biosciences (Shanghai, China). The expression vector GV230 containing the target sequence of Spry3 and the control vector GV170 containing the whole coding sequence of psiCHECK-2 were synthesized by Aiji Biotechnology (Guangzhou, China). Plasmid DNAs were purified with a TIANprep mini plasmid kit (Tiangen, China). All transfection assays including microRNA and plasmid DNA were performed using Lipofectamine 2000 reagent (Invitrogen, USA). The cells were harvested for qPCR or western blotting after 48 or 72 h of transfection individually. MicroRNA mimics, agomiRs, inhibitors, and antagomiRs were transfected at 50 nmol/L with Lipofectamine 2000 reagent (Invitrogen, USA).

Exosome Isolation

To isolate exosomes from different transfected HUVECs, supernatants were collected from cells and centrifuged at 1,500 × *g* for 15 min to remove cells and at 10,000 × *g* for 30 min to deplete residual cellular debris. Afterward, samples were serially filtered through 0.45- and 0.22-μm filters. The filtered supernatant was serially centrifuged at 100,000 × *g* for 70 min, 100, 000 × *g* for 60 min, and 100,000 × *g* for 70 min. After isolation, exosomes were re-suspended in a moderate amount of PBS and stored at −80°C before use. The above procedures were carried out at 4°C or on ice.

Characterization of Exosomes

The particle size of exosomes was assessed using dynamic laser light scattering (DLS; Zetasizer Nano-ZS, Malvern Panalytical, UK). Procedures were conducted at 25°C after equilibration for 10 s according to the manufacturer's instructions. Morphology and particle size of exosomes were further assessed via transmission electronic microscopy (TEM; Hitachi HC-1, Japan) with an accelerating voltage of 80 kV.

Exosome labeling

The fluorescent dyes DiI and DiD (Invitrogen, USA) were used to label exosomes *in vitro* or *in vivo*. Purified exosomes were incubated in the presence of each fluorescent dye (5 mM DiI *in vitro*, 5 mM DiD *in vivo*), stirred for 4 h at room temperature (RT), and then ultracentrifuged at 100,000 × *g* for 70 min to deplete free dye. Afterward, the labeled exosomes were resuspended in moderate PBS and stored at −80°C before use.

Identification of iRGD Expression on Exosomes

To explore the specific binding activity of iRGD-exo to αvβ3, the αvβ3-coated wells were pre-incubated with a synthetic iRGD peptide that demonstrates competitive binding to αvβ3. Briefly, purified αvβ3 integrins (Millipore, USA) were immobilized in the wells of microtiter plates (1–5 μg/mL, 50 μL/well) by adsorption overnight before blocking with casein blocker (Pierce, UK). DiI-labeled exosomes were then resuspended using binding buffer including 50 mM Tris (pH 8.0), 150 mM NaCl, 1 mM $MgCl_2$, 1 mM $CaCl_2$, and 0.5 mM $MnCl_2$, and then added to the microtiter wells. After incubation for 2 h, the unbound dyes and exosomes were depleted by washing the wells with the binding buffer three times. Bound exosomes were then quantitated by detecting the fluorescence intensity at an excitation wavelength of 484 nm and an emission wavelength of 501 nm.

Western Blotting

After treatment with siRNA negative control (si-NC), si-Spry3, agomiR-NC, agomiR-18a, agomiR-BART10-5p, agomiR-18a combined agomiR-BART10-5p, antagomiR-NC, antagomiR-18a, antagomiR-BART10-5p, and antagomiR-18a combined antagomiR-BART10-5p, HONE1 and HONE1-EBV cells were harvested and lysed in lysis buffer supplemented with protease inhibitors. MicroRNA mimics, agomiRs, inhibitors, and antagomiRs were transfected at 50 nmol/L with Lipofectamine 2000 reagent (Invitrogen, USA). Protein lysate was resolved on 10% SDS-PAGE followed by blot transfer onto a polyvinylidene fluoride (PVDF) membrane (Millipore, USA) using the semidry NovaBlot system (Amersham Pharmacia, UK) for western blot analysis. After that, the membranes were first incubated with antibodies against GAPDH (Proteintech, USA), Spry3, Ras, c-Raf, MEK1/2, Erk1/2, mTOR, eIF4E1, VEGF, mmp2, and HIF1-α (Abcam, UK) overnight at 4°C, followed by a 1- to 2-h incubation with horseradish peroxidase-conjugated secondary antibody. The protein signals were detected using an enhanced chemiluminescence kit (Fdbio Science, China) and analyzed using the Bio-Rad (USA) imaging system and the associated software according to the manufacturer's instructions. Antibodies concentrations are listed in Table S1.

Tube Formation Assay

50 μL of Matrigel (BD Biosciences, USA) was added to each well of a 96-well plate and allowed to polymerize. HUVECs were suspended in the medium at a density of 3×10^5 cells/mL, and 0.1 mL of the transfected cell supernatant (100 μL of transfection concentration 50 nmol/L or 50 μg of iRGD-exo) was added to each well coated with Matrigel, together with or without the indicated recombinant proteins. Cells were incubated for 4–8 hours at 37°C. Afterward, cells were imaged, and branch points from four to six high-power fields (HPFs) (×200) were counted and averaged.

CAM Assay

For CAM assays, white Leghorn chicken eggs (South China Agricultural University, Guangzhou, China) were incubated under routine conditions (constant humidity and 37°C), and a square window was opened in the eggshell at day 3 of incubation, after removal of 3.5 mL of albumen to detach the shell from the developing CAM. The window was sealed with a glass of the same size, and the eggs were returned to the incubator. Gelatin sponges were cut to a size of 1 mm^3 and placed on top of the CAM at day 8 under sterile conditions. The sponges were then absorbed with moderate transfected cell supernatants (200 μL of transfection concentration 50 nmol/L) or 100 μg of iRGD-exo to be tested. CAMs were examined daily and imaged with a digital camera at day 12. The area of blood vessels accounting for the whole CAM was determined with an Image-Pro Plus 6 analysis system.

Matrigel Plug Assay

For Matrigel plug assays, Matrigel (0.5 mL/plug) with bFGF (4 ng/mL) and different transfected cell supernatants (200 μL of transfection concentration 50 nmol/L) in liquid form at 4°C were respectively injected subcutaneously (s.c.) in the midventral abdominal region of 4- to 5-week-old athymic nude male nu/nu mice. Each group had four to five Matrigel plugs. After 8 days, the mice were sacrificed, and the plugs were removed for hemoglobin analysis and immunohistochemistry staining. The Matrigel plugs were examined for hemoglobin content using the Quanti-Chrom hemoglobin assay kit following the manufacturer's protocol (BioAssay Systems, USA). For immunohistochemistry staining, the Matrigel plugs were fixed by 4% paraformaldehyde and embedded with paraffin. Afterward, the 5-mm serial sections were performed with immunohistochemistry staining for microvessel density (CD31) analysis. The area of microvessel density in a HPF (×200) was counted with Image-Pro Plus 6 analysis software.

Confocal Microscope Examinations

HONE1 and HONE1-EBV cells were seeded on sterile coverslips with monolayer on the day before staining. Then, the cells were incubated with DiI-labeled exosomes (60 μg of iRGD-exo) shielded from light for 4 h at 37°C. Cells were then washed with pre-cooled PBS three times, each for 5 min, fixed with 4% formaldehyde for 10–15 min at room temperature, and washed with PBS three times, each for 5 min. Subsequently, cells were stained for nuclei with Hoechst 33342 (Beyotime, China) for 3–5 min, and then washed with PBS three times, each for 5 min. The coverslips were mounted on slides using anti-fade mounting medium (Beyotime, China) mixed with neutralizing antibodies (Solarbio Life Sciences, China). Confocal images were acquired on a Zeiss LSM880 (Zeiss, Germany) confocal micrograph system.

Luciferase Reporter Assay

Spry3 was predicted to be directly co-regulated by BART10-5p and miR-18a with the bioinformatics websites BiBiserv2 and RNAhybrid. For miR-18a, a fragment of Spry3 3′ UTR amplified by PCR primers was cloned into psiCHECK-2 vectors (named WT). The primer sequences are as follows: Spry3 mut (for miR-18a), forward, 5′-GTACGGAATCCTCATCTTCAAAGTC-3′, reverse, 5′-CTTCTAGGGCCTTAGGACACAGGTTC-3′; and Spry3 mut (for BART10-5p), forward, GAGGGGACCTCCATGTCCCTTTGTTG-3′, reverse, 5′-TTCCCCCCGTGTACTACTATACAC-3′. Site-directed mutagenesis of the miR-18a binding site in the Spry3 3′ UTR (named mut) was performed using a GeneTailor site-directed mutagenesis system (Invitrogen, USA). For luciferase reporter assays, WT or mut vector and the control vector psiCHECK-2 vector were co-transfected into 293T cells with miR-18a mimics or inhibitor (transfection concentration, 50 nmol/L) using Lipofectamine 2000 reagent (Invitrogen, USA). After 48 h of transfection, luciferase activity was detected taking advantage of the Dual-Luciferase reporter assay system (GeneCopoeia, USA). The y axis is relative luciferase activity, and the means represent the ratio of Renilla luciferase optical densities (ODs) to firefly luciferase ODs. For BART10-5p, the verification of target gene Spry3 was similar to the above process utilizing the luciferase reporter assay.

In Vivo Antiangiogenesis and Therapeutic Assay

All *in vivo* experiments were approved by the Animal Research Committee of Southern Medical University in accordance with the National Institutes of Health *Guide for the Care and Use of Laboratory Animals* (NIH publication no. 8023, revised 1978). Animals received humane care according to the above institutional guidelines. Animals on a standard diet were maintained in a specific pathogen-free animal facility with a 12-h light/12-h dark cycle. Athymic nude male nu/nu mice (Central Animal Facility of Southern Medical University, 4–5 weeks old) were injected with 200 μL of the EBV-positive NPC cell line (HONE1-EBV, 3×10^6) on the right flank. Tumors were allowed to grow for 3–5 days and then mice were randomly divided into seven groups (five per group), and the groups were treated as follows: (1) free exosomes, as a control; (2) exo-antagomiR-18a; (3) exo-antagomiR-BART10-5p; (4) exo-antagomiR-18a and exo-antagomiR-BART10-5p; (5) iRGD-exo-antagimiR-18a; (6) iRGD-exo-antagimiR-BART10-5p; and (7) iRGD-exo-antagimiR-18a and iRGD-exo-antagimiR-BART10-5p. The tumors were allowed to grow for 14–16 days until their size reached between 200 and 600 mm^3. The doses (each at an equivalent dose of 150 μg of exosomes) were injected at 1-day intervals. Tumor length (L), width (W), and body weight were recorded at 1-day intervals. Tumor weight was calculated according to the formula $(L \times W^2)/2$.

Immunohistochemistry Staining

Matrigel plug and xenograft tissues were fixed in 4% paraformaldehyde for 1–2 days before the experiment. Serial sections (5 mm thick) were deparaffinized in xylene and rehydrated through descending percentages of ethanol to water. Subsequently, antigen retrieval was conducted with 10 mM citrate buffer (pH 6.0). For microvessel density analysis, sections were incubated with the CD31 antibody (Abcam, 1:500). Detection was done with diaminobenzidine chromogen, which results in brown color staining. Hematoxylin was applied to counterstain the cell nuclei.

Statistical Analysis

Statistical analysis was performed using the SPSS 16.0 statistical software package (SPSS, Chicago, IL, USA). Differences were considered to be statistically significant at values of $p < 0.05$ with a Student's t test for two groups, one-way ANOVA (analysis of variance) analysis for multiple groups, and a parametric generalized linear model with random effects for tumor growth. All data were derived from at least three independent experiments and are presented as a mean value with its standard deviation indicated (mean ± SD). Differences were considered significance at $^{*}p < 0.05$, $^{**}p < 0.01$, $^{***}p < 0.001$.

SUPPLEMENTAL INFORMATION

Supplemental Information can be found online at https://doi.org/10.1016/j.omtn.2020.08.017.

AUTHOR CONTRIBUTIONS

This study was designed and supervised by X. Li. and X. Lyu. J.W., Q.J., O.D.F., C.-M.T., M.Z., G.W., S.-W.T., M.F., Y.C., and T.D. generated mouse models, performed experiments *in vivo* and *in vitro*, and analyzed the data. T.C., Y.L., X.Y., Y.Z., Y.C., H.L., and M. P. supervised and performed patient tissue collection and histological and immunohistochemistry data analysis. The manuscript was written by X. Li. and X. Lyu and was approved by all authors.

CONFLICTS OF INTEREST

The authors declare no competing interests.

ACKNOWLEDGMENTS

This work was funded by grants from the National Natural Science Foundation of China (nos. 81572644, 81502335, and 81902761); the NSFC/RGC Joint Research Project (nos. N_HKU735/18 and 81861168033); the China Postdoctoral Science Foundation (no. 2016M602493); the Natural Science Foundation of Guangdong Province (no. 2020A1515010081); the Shenzhen Key Laboratory of Viral Oncology (no. ZDSYS201707311140430); the Shenzhen Science and Technology Key Project (no. JCYJ20170413165531148); the Science and Technology Program of Guangzhou, China (no. 201704020127); and from the Anhui Provincial Natural Science Foundation, China (no. 1908085QH330). Finally, we are very grateful to the Sanming Project of Medicine in Shenzhen (no. SZSM201612023) for the contribution to this research.

REFERENCES

1. Krump, N.A., and You, J. (2018). Molecular mechanisms of viral oncogenesis in humans. Nat. Rev. Microbiol. *16*, 684–698.
2. Ronca, R., Benkheil, M., Mitola, S., Struyf, S., and Liekens, S. (2017). Tumor angiogenesis revisited: regulators and clinical implications. Med. Res. Rev. *37*, 1231–1274.
3. Hanahan, D., and Weinberg, R.A. (2011). Hallmarks of cancer: the next generation. Cell *144*, 646–674.
4. DiMaio, T.A., Gutierrez, K.D., and Lagunoff, M. (2014). Kaposi's sarcoma-associated herpesvirus downregulates transforming growth factor β2 to promote enhanced stability of capillary-like tube formation. J. Virol. *88*, 14301–14309.
5. Eskander, R.N., and Tewari, K.S. (2014). Targeting angiogenesis in advanced cervical cancer. Ther. Adv. Med. Oncol. *6*, 280–292.
6. Yoshizaki, T., Kondo, S., Endo, K., Nakanishi, Y., Aga, M., Kobayashi, E., Hirai, N., Sugimoto, H., Hatano, M., Ueno, T., et al. (2018). Modulation of the tumor microenvironment by Epstein-Barr virus latent membrane protein 1 in nasopharyngeal carcinoma. Cancer Sci. *109*, 272–278.
7. Ribatti, D., Nico, B., Ranieri, G., Specchia, G., and Vacca, A. (2013). The role of angiogenesis in human non-Hodgkin lymphomas. Neoplasia *15*, 231–238.
8. Nienhüser, H., and Schmidt, T. (2017). Angiogenesis and anti-angiogenic therapy in gastric cancer. Int. J. Mol. Sci. *19*, 1.
9. Trang, P., Weidhaas, J.B., and Slack, F.J. (2017). MicroRNAs and cancer. In The Molecular Basis of Human Cancer, W.B. Coleman and G.J. Tsongalis, eds. (Springer), pp. 277–286.
10. Rupaimoole, R., and Slack, F.J. (2017). MicroRNA therapeutics: towards a new era for the management of cancer and other diseases. Nat. Rev. Drug Discov. *16*, 203–222.
11. Tiwari, A., Mukherjee, B., and Dixit, M. (2018). MicroRNA key to angiogenesis regulation: miRNA biology and therapy. Curr. Cancer Drug Targets *18*, 266–277.
12. Peng, Y., and Croce, C.M. (2016). The role of MicroRNAs in human cancer. Signal Transduct. Target. Ther. *1*, 15004.
13. Wang, Y., Wang, L., Chen, C., and Chu, X. (2018). New insights into the regulatory role of microRNA in tumor angiogenesis and clinical implications. Mol. Cancer *17*, 22.
14. Hsu, Y.L., Hung, J.Y., Chang, W.A., Jian, S.F., Lin, Y.S., Pan, Y.C., Wu, C.Y., and Kuo, P.L. (2018). Hypoxic lung-cancer-derived extracellular vesicle microRNA-103a increases the oncogenic effects of macrophages by targeting PTEN. Mol. Ther. *26*, 568–581.
15. O'Loghlen, A. (2018). Role for extracellular vesicles in the tumour microenvironment. Philos. Trans. R. Soc. Lond. B Biol. Sci. *373*, 373.
16. Tsao, S.W., Tsang, C.M., To, K.F., and Lo, K.W. (2015). The role of Epstein-Barr virus in epithelial malignancies. J. Pathol. *235*, 323–333.
17. Xiang, T., Lin, Y.X., Ma, W., Zhang, H.J., Chen, K.M., He, G.P., Zhang, X., Xu, M., Feng, Q.S., Chen, M.Y., et al. (2018). Vasculogenic mimicry formation in EBV-associated epithelial malignancies. Nat. Commun. *9*, 5009.
18. Cai, L.M., Lyu, X.M., Luo, W.R., Cui, X.F., Ye, Y.F., Yuan, C.C., Peng, Q.X., Wu, D.H., Liu, T.F., Wang, E., et al. (2015). EBV-miR-BART7-3p promotes the EMT and metastasis of nasopharyngeal carcinoma cells by suppressing the tumor suppressor PTEN. Oncogene *34*, 2156–2166.
19. Lyu, X., Wang, J., Guo, X., Wu, G., Jiao, Y., Faleti, O.D., Liu, P., Liu, T., Long, Y., Chong, T., et al. (2018). EBV-miR-BART1-5P activates AMPK/mTOR/HIF1 pathway via a PTEN independent manner to promote glycolysis and angiogenesis in nasopharyngeal carcinoma. PLoS Pathog. *14*, e1007484.
20. Lo, A.K.F., To, K.F., Lo, K.W., Lung, R.W., Hui, J.W., Liao, G., and Hayward, S.D. (2007). Modulation of LMP1 protein expression by EBV-encoded microRNAs. Proc. Natl. Acad. Sci. USA *104*, 16164–16169.
21. Lung, R.W.M., Tong, J.H.M., Sung, Y.M., Leung, P.S., Ng, D.C.H., Chau, S.L., Chan, A.W., Ng, E.K., Lo, K.W., and To, K.F. (2009). Modulation of LMP2A expression by a newly identified Epstein-Barr virus-encoded microRNA miR-BART22. Neoplasia *11*, 1174–1184.
22. Cao, S., Durrani, F.A., Toth, K., Rustum, Y.M., and Seshadri, M. (2011). Bevacizumab enhances the therapeutic efficacy of Irinotecan against human head and neck squamous cell carcinoma xenografts. Oral Oncol. *47*, 459–466.

23. Yoo, D.S., Kirkpatrick, J.P., Craciunescu, O., Broadwater, G., Peterson, B.L., Carroll, M.D., Clough, R., MacFall, J.R., Hoang, J., Scher, R.L., et al. (2012). Prospective trial of synchronous bevacizumab, erlotinib, and concurrent chemoradiation in locally advanced head and neck cancer. Clin. Cancer Res. *18*, 1404–1414.

24. Cai, L., Ye, Y., Jiang, Q., Chen, Y., Lyu, X., Li, J., Wang, S., Liu, T., Cai, H., Yao, K., et al. (2015). Epstein-Barr virus-encoded microRNA BART1 induces tumour metastasis by regulating PTEN-dependent pathways in nasopharyngeal carcinoma. Nat. Commun. *6*, 7353.

25. Mogilyansky, E., and Rigoutsos, I. (2013). The miR-17/92 cluster: a comprehensive update on its genomics, genetics, functions and increasingly important and numerous roles in health and disease. Cell Death Differ. *20*, 1603–1614.

26. Fang, L., Deng, Z., Shatseva, T., Yang, J., Peng, C., Du, W.W., Yee, A.J., Ang, L.C., He, C., Shan, S.W., and Yang, B.B. (2011). MicroRNA miR-93 promotes tumor growth and angiogenesis by targeting integrin-β8. Oncogene *30*, 806–821.

27. Luo, Z., Dai, Y., Zhang, L., Jiang, C., Li, Z., Yang, J., McCarthy, J.B., She, X., Zhang, W., Ma, J., et al. (2013). miR-18a promotes malignant progression by impairing microRNA biogenesis in nasopharyngeal carcinoma. Carcinogenesis *34*, 415–425.

28. Chen, X., Wang, J., Cheng, L., and Lu, M.P. (2014). miR-18a downregulates DICER1 and promotes proliferation and metastasis of nasopharyngeal carcinoma. Int. J. Clin. Exp. Med. *7*, 847–855.

29. Hsu, C.Y., Yi, Y.H., Chang, K.P., Chang, Y.S., Chen, S.J., and Chen, H.C. (2014). The Epstein-Barr virus-encoded microRNA miR-BART9 promotes tumor metastasis by targeting E-cadherin in nasopharyngeal carcinoma. PLoS Pathog. *10*, e1003974.

30. Nachmani, D., Stern-Ginossar, N., Sarid, R., and Mandelboim, O. (2009). Diverse herpesvirus microRNAs target the stress-induced immune ligand MICB to escape recognition by natural killer cells. Cell Host Microbe *5*, 376–385.

31. Chan, J.Y., Gao, W., Ho, W.K., Wei, W.I., and Wong, T.S. (2012). Overexpression of Epstein-Barr virus-encoded microRNA-BART7 in undifferentiated nasopharyngeal carcinoma. Anticancer Res. *32*, 3201–3210.

32. Yan, Q.J., Zeng, Z., Gong, Z., Zhang, W., Gong, Z.J., Zhang, W.L., et al. (2015). EBV-miR-BART10-3p facilitates epithelial-mesenchymal transition and promotes metastasis of nasopharyngeal carcinoma by targeting BTRC. Oncotarget *6*, 41766–41782.

33. Nachmani, D., Lankry, D., Wolf, D.G., and Mandelboim, O. (2010). The human cytomegalovirus microRNA miR-UL112 acts synergistically with a cellular microRNA to escape immune elimination. Nat. Immunol. *11*, 806–813.

34. Hacohen, N., Kramer, S., Sutherland, D., Hiromi, Y., and Krasnow, M.A. (1998). Sprouty encodes a novel antagonist of FGF signaling that patterns apical branching of the *Drosophila* airways. Cell *92*, 253–263.

35. Casci, T., Vinós, J., and Freeman, M. (1999). Sprouty, an intracellular inhibitor of Ras signaling. Cell *96*, 655–665.

36. Mason, J.M., Morrison, D.J., Basson, M.A., and Licht, J.D. (2006). Sprouty proteins: multifaceted negative-feedback regulators of receptor tyrosine kinase signaling. Trends Cell Biol. *16*, 45–54.

37. Kramer, S., Okabe, M., Hacohen, N., Krasnow, M.A., and Hiromi, Y. (1999). Sprouty: a common antagonist of FGF and EGF signaling pathways in Drosophila. Development *126*, 2515–2525.

38. Lao, D.H., Chandramouli, S., Yusoff, P., Fong, C.W., Saw, T.Y., Tai, L.P., Yu, C.Y., Leong, H.F., and Guy, G.R. (2006). A Src homology 3-binding sequence on the C terminus of Sprouty2 is necessary for inhibition of the Ras/ERK pathway downstream of fibroblast growth factor receptor stimulation. J. Biol. Chem. *281*, 29993–30000.

39. Jones, N., Iljin, K., Dumont, D.J., and Alitalo, K. (2001). Tie receptors: new modulators of angiogenic and lymphangiogenic responses. Nat. Rev. Mol. Cell Biol. *2*, 257–267.

40. Mason, J.M., Morrison, D.J., Bassit, B., Dimri, M., Band, H., Licht, J.D., and Gross, I. (2004). Tyrosine phosphorylation of Sprouty proteins regulates their ability to inhibit growth factor signaling: a dual feedback loop. Mol. Biol. Cell *15*, 2176–2188.

41. Sasaki, A., Taketomi, T., Wakioka, T., Kato, R., and Yoshimura, A. (2001). Identification of a dominant negative mutant of Sprouty that potentiates fibroblast growth factor- but not epidermal growth factor-induced ERK activation. J. Biol. Chem. *276*, 36804–36808.

42. Kalluri, R. (2016). The biology and function of exosomes in cancer. J. Clin. Invest. *126*, 1208–1215.

43. Tkach, M., and Théry, C. (2016). Communication by extracellular vesicles: where we are and where we need to go. Cell *164*, 1226–1232.

44. Alvarez-Erviti, L., Seow, Y., Yin, H., Betts, C., Lakhal, S., and Wood, M.J. (2011). Delivery of siRNA to the mouse brain by systemic injection of targeted exosomes. Nat. Biotechnol. *29*, 341–345.

45. Liao, W., Du, Y., Zhang, C., Pan, F., Yao, Y., Zhang, T., and Peng, Q. (2019). Exosomes: the next generation of endogenous nanomaterials for advanced drug delivery and therapy. Acta Biomater. *86*, 1–14.

46. Jeppesen, D.K., Fenix, A.M., Franklin, J.L., Higginbotham, J.N., Zhang, Q., Zimmerman, L.J., Liebler, D.C., Ping, J., Liu, Q., Evans, R., et al. (2019). Reassessment of exosome composition. Cell *177*, 428–445.e18.

47. Tian, Y., Li, S., Song, J., Ji, T., Zhu, M., Anderson, G.J., Wei, J., and Nie, G. (2014). A doxorubicin delivery platform using engineered natural membrane vesicle exosomes for targeted tumor therapy. Biomaterials *35*, 2383–2390.

OMTN, Volume *22*

Supplemental Information

Exosomal Delivery of AntagomiRs Targeting Viral and Cellular MicroRNAs Synergistically Inhibits Cancer Angiogenesis

Jianguo Wang, Qiang Jiang, Oluwasijibomi Damola Faleti, Chi-Man Tsang, Min Zhao, Gongfa Wu, Sai-Wah Tsao, Minyi Fu, Yuxiang Chen, Tengteng Ding, Tuotuo Chong, Yufei Long, Xu Yang, Yuanbin Zhang, Yunxi Cai, Hanzhao Li, Manli Peng, Xiaoming Lyu, and Xin Li

Supplemental Figures and Legends:

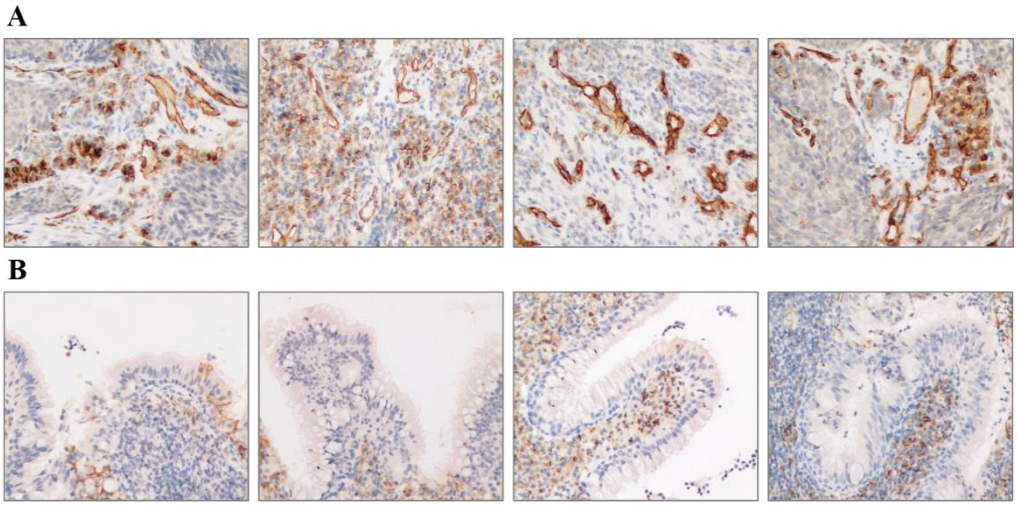

Figure S1 The expression of CD31 in NPC (A) and NP (B) (200x).

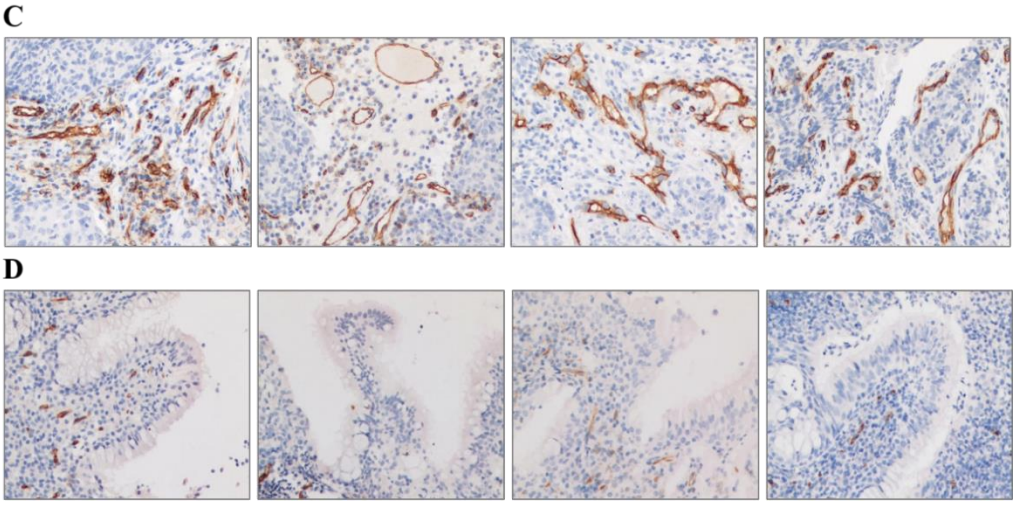

Figure S1 The expression of CD34 in NPC (C) and NP (D) (200x).

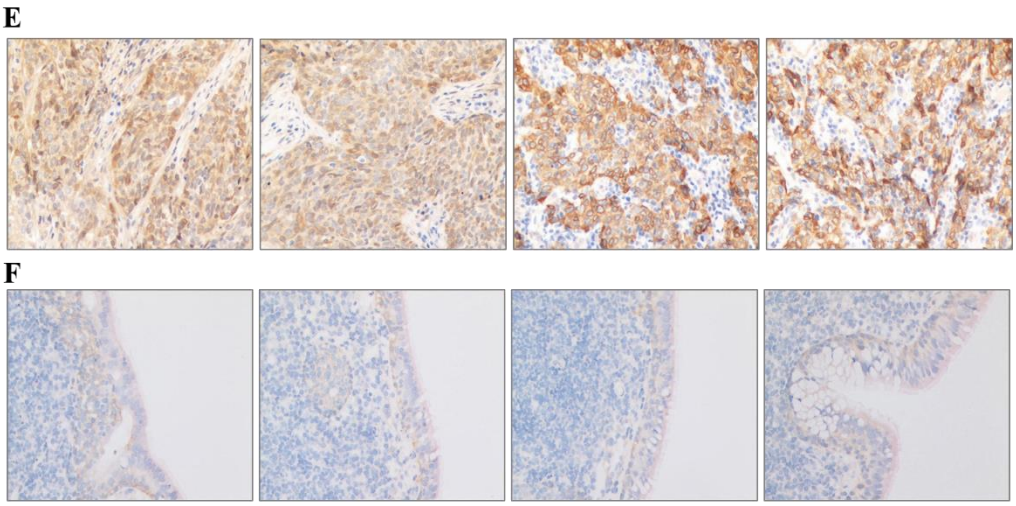

Figure S1 The expression of αv in NPC (E) and NP (F) (200x).

G

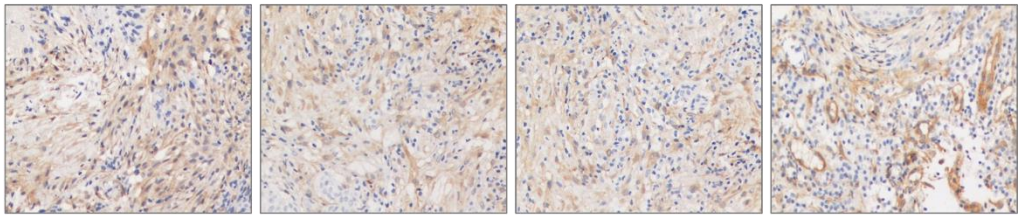

H

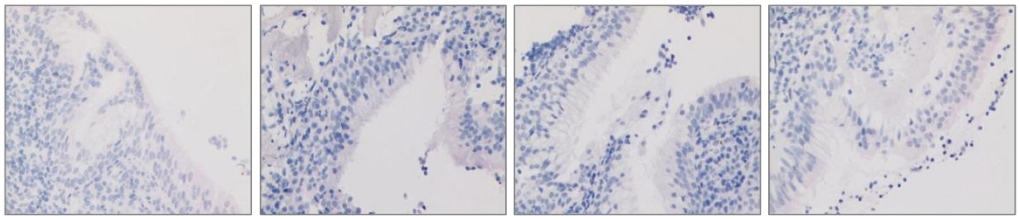

Figure S1 The expression of β3 in NPC (G) and NP (H) (200x).

I

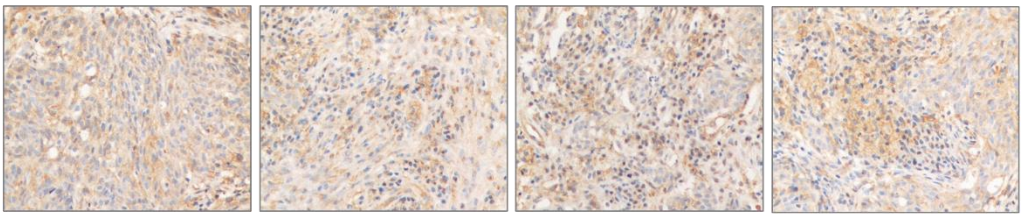

J

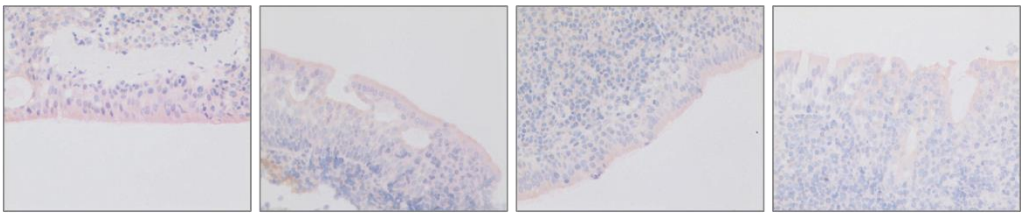

Figure S1 The expression of VEGFR1 in NPC (I) and NP (J) (200x).

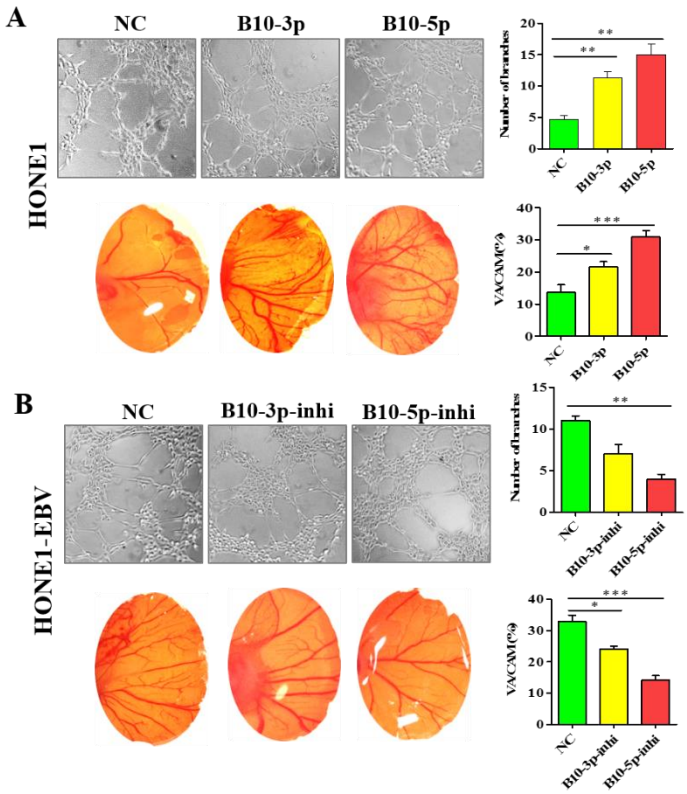

Figure S2 EBV-miR-BART10-5p possesses a superior angiogenesis-promoting effect compared with EBV-miR-BART10-3p.

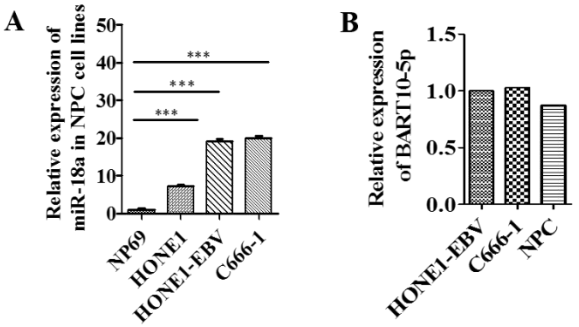

Figure S3 Expression of BART10-5p and miR-18a in NPC cell or NPC tissues.

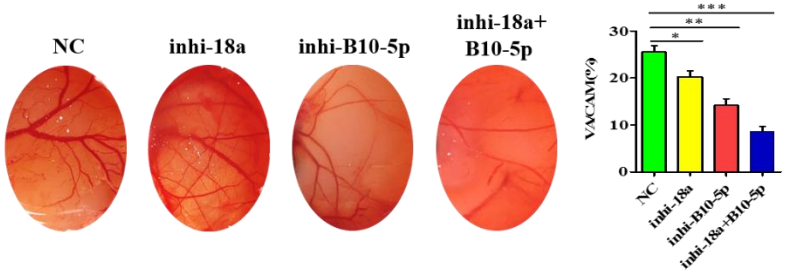

Figure S4 Influence upon angiogenesis after inhibition of BART10-5p and miR-18a in NPC C666-1 cell .

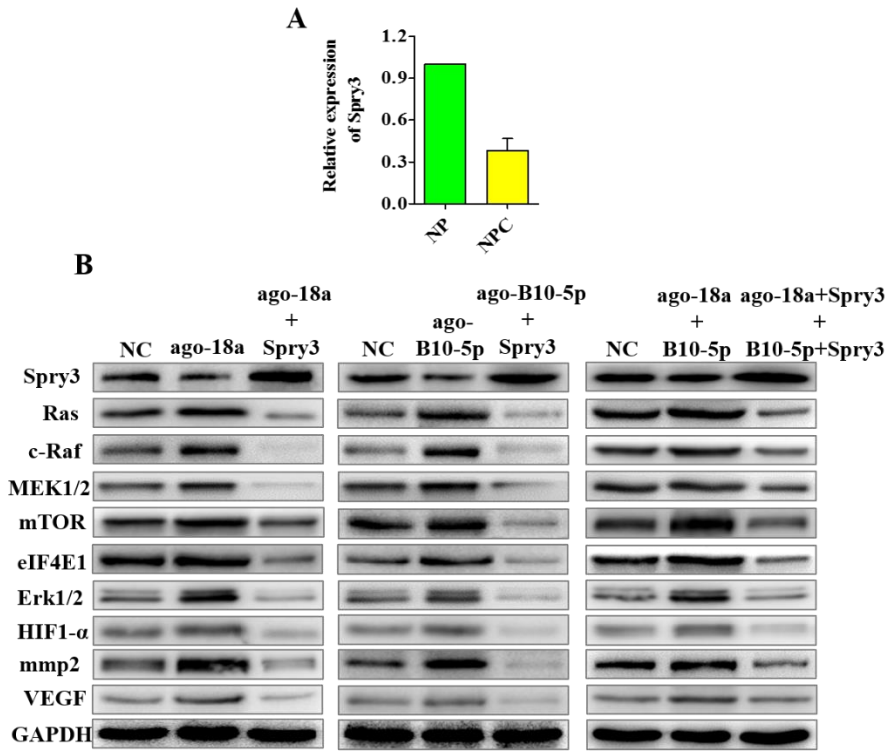

Figure S5A Expression of Spry3 in NPC tissues; Figure S5B Influence upon angiogenesis-associated pathway after recovery of Spry3.

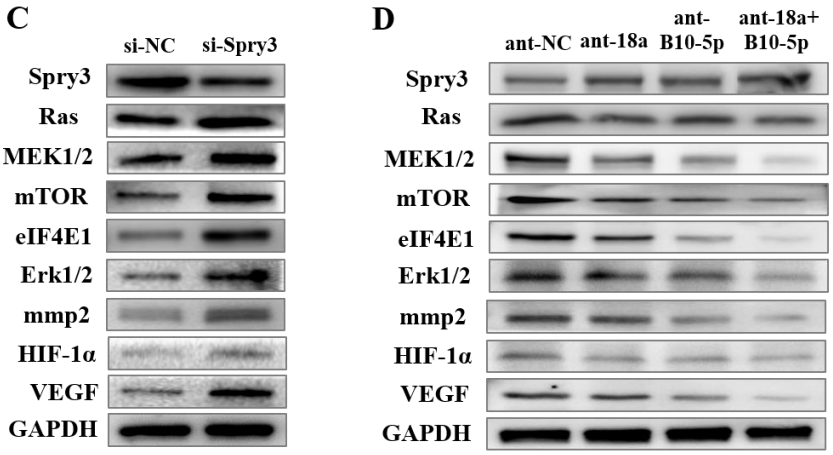

Figure S5C, S5D Influence upon angiogenesis-associated pathway after inhibition of Spry3, miR-18a, BART10-5p in C666-1 cells.

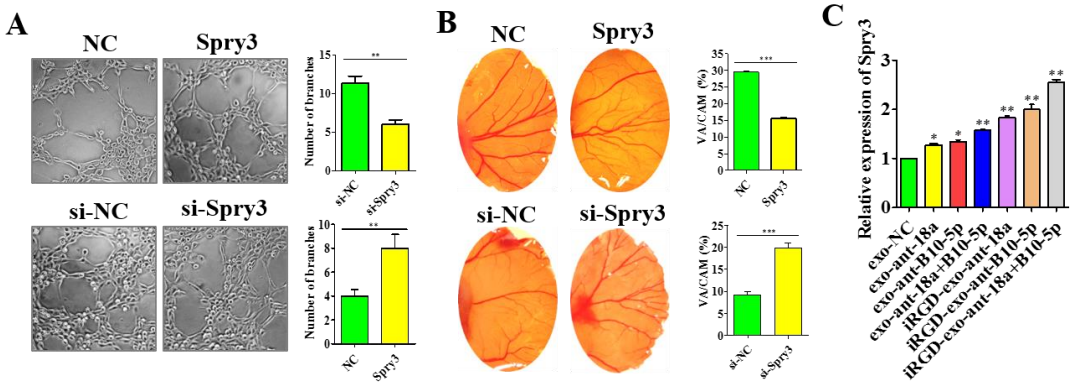

Figure S6 Spry3 is closely linked with angiogenesis in NPC.

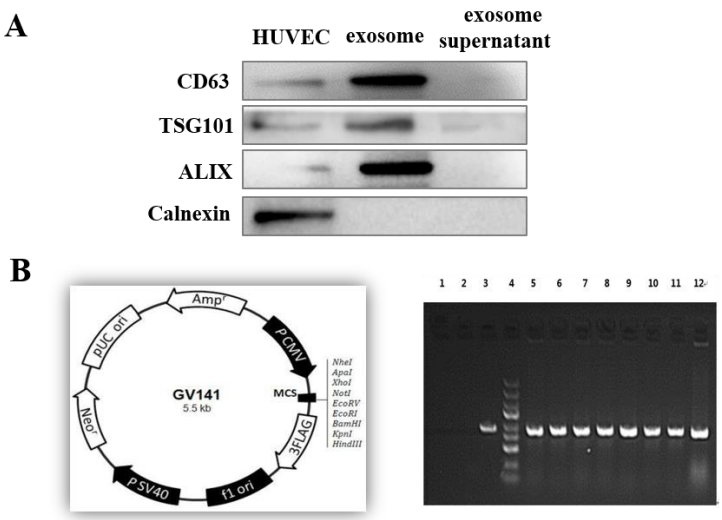

Figure S7A Identification of protein markers in exosome;
Figure S7B Construction of iRGD-Lamp2b plasmid.

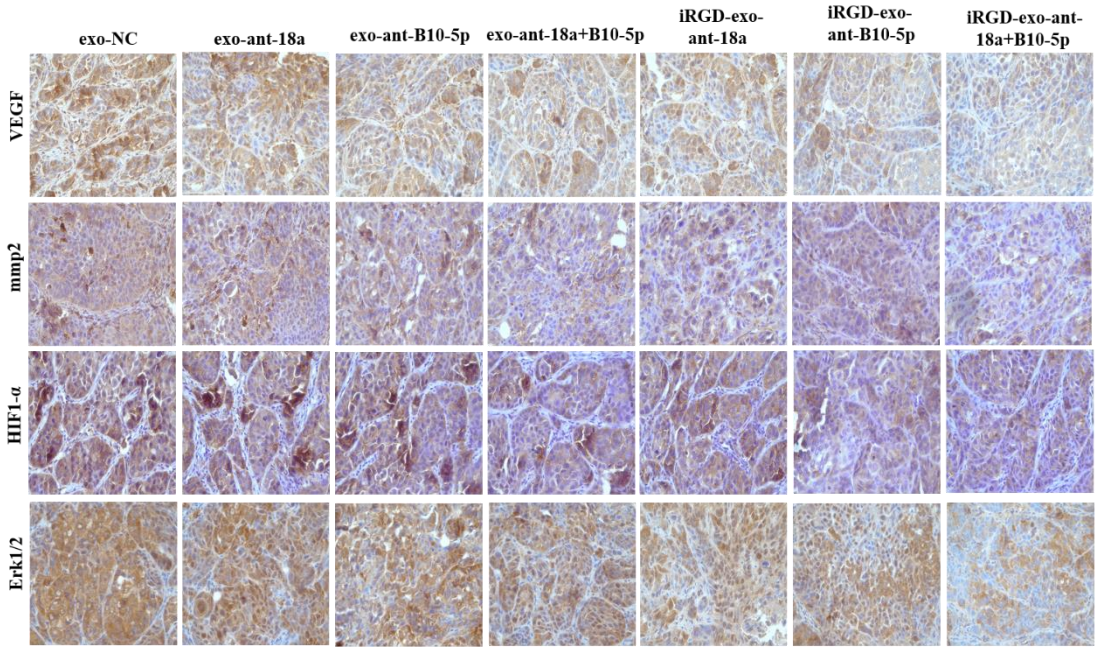

Figure S8 Down-regulation of regulating factors namely; VEGF, mmp2, HIF1-α, and Erk1/2 which are downstream of Spry3 in iRGD-exo-antagomiRs groups compared the free exosome control or exo-antagomiRs groups.

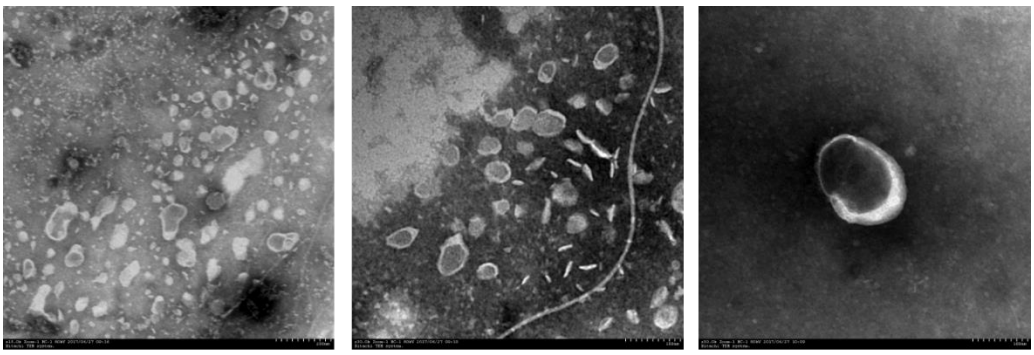

Figure S9 TAM of exosome.

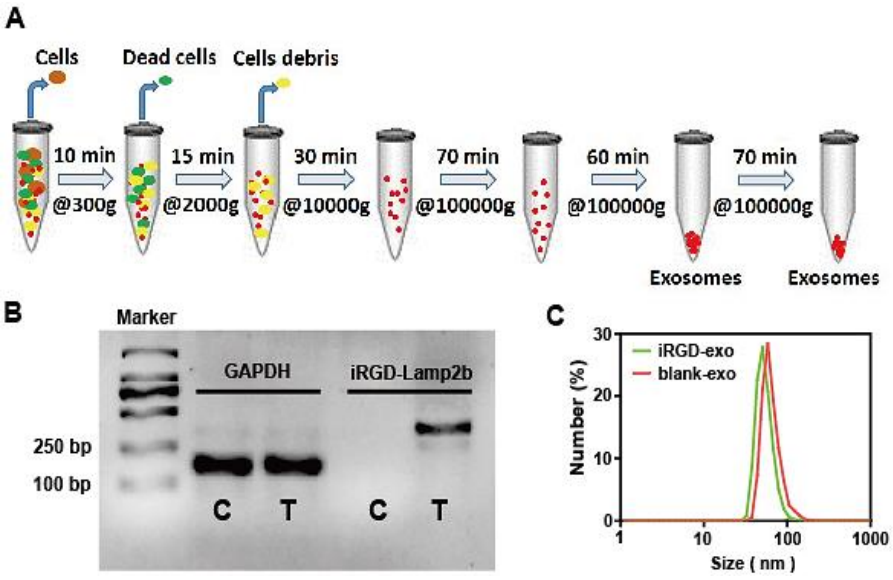

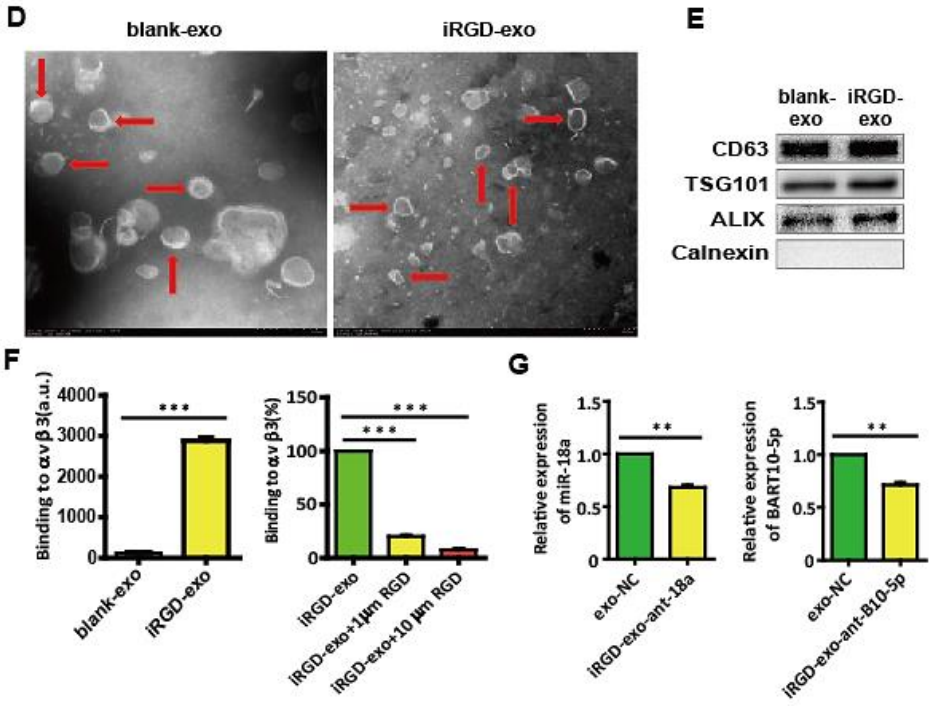

Figure S10. Isolation, identification, and characterization of exosomes.

(A) Schematic representation of isolating exosomes from the culture supernatant of HUVECs. (B) mRNA expression level of iRGD-Lamp2b in transfected HUVECs. (C) The size distributions of control (blank-exo) and iRGD-positive (iRGD-exo) exosomes. (D) Representative TEM images of control (blank-exo) and iRGD-positive (iRGD-exo) exosomes. Scale bar = 200 nm (in the lower right corner). (E) Expressions of CD63, ALIX, TSG101 and Calnexin in control (blank-exo) and iRGD-positive (iRGD-exo) exosomes derived from HUVECs. (F) Binding activity of blank-exo or iRGD-exo to immobilized αvβ3 integrin(left). (G) The relative expressions of BART10-5p and miR-18a following isolation of exosomes from co-transfection of BART10-5p/miR-18a and Lamp2b-iRGD in HUVEC.

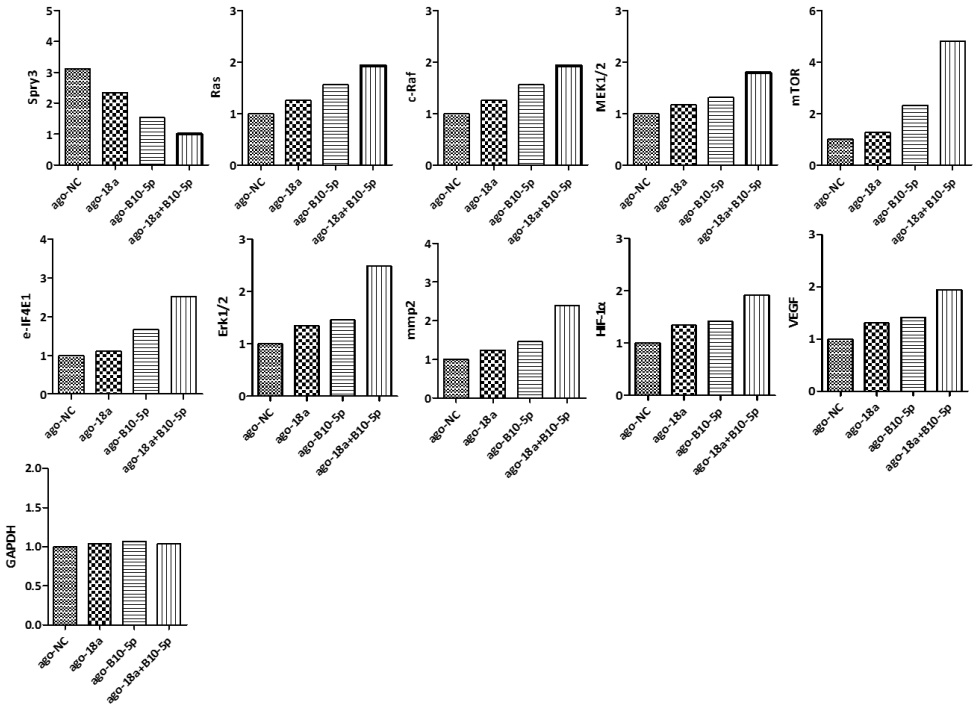

Figure S11 Quantitative analysis of western blot results by using Image J for Figure 3D .

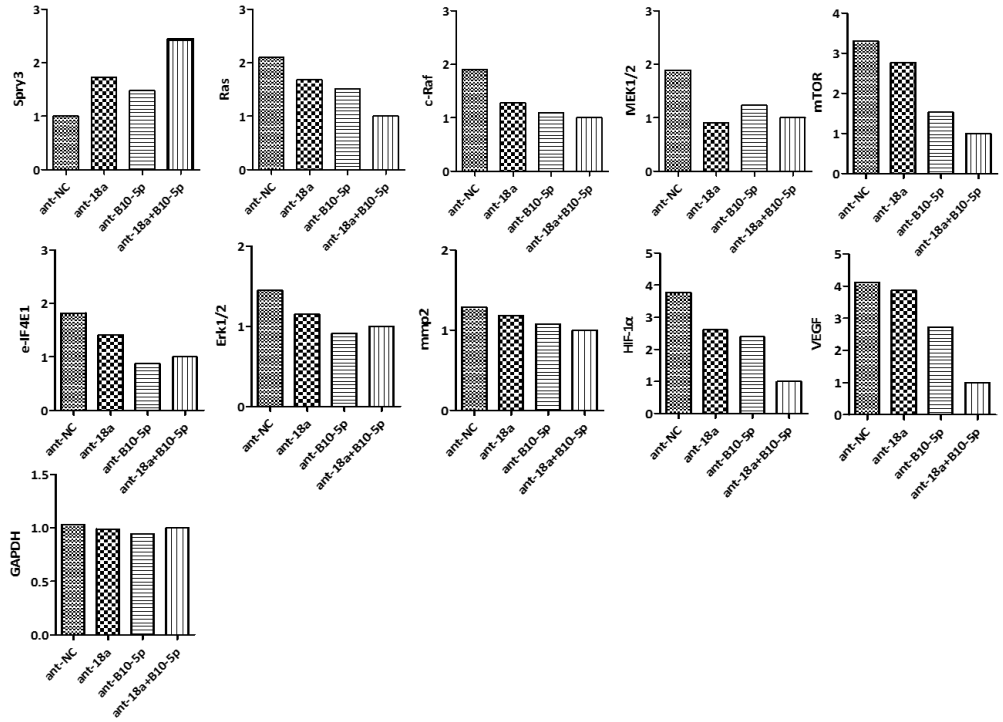

Figure S12 Quantitative analysis of western blot result by using Image J for Figure 3E .

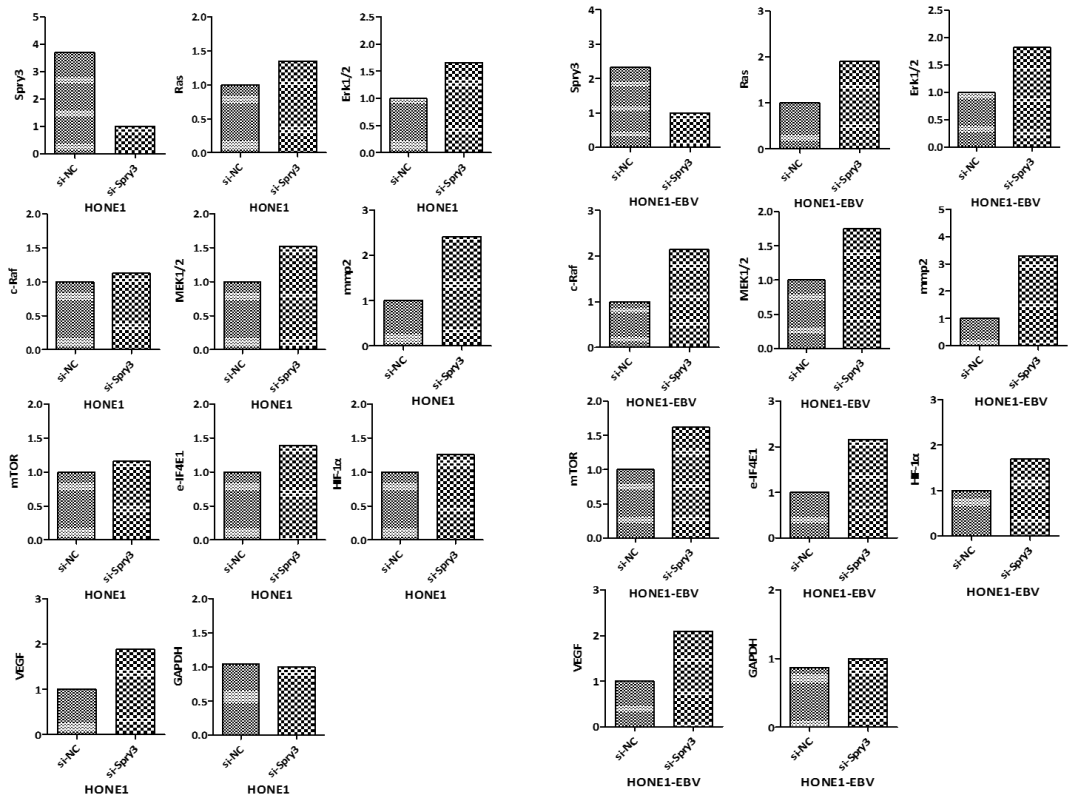

Figure S13 Quantitative analysis of western blot result by using Image J for Figure 3F .

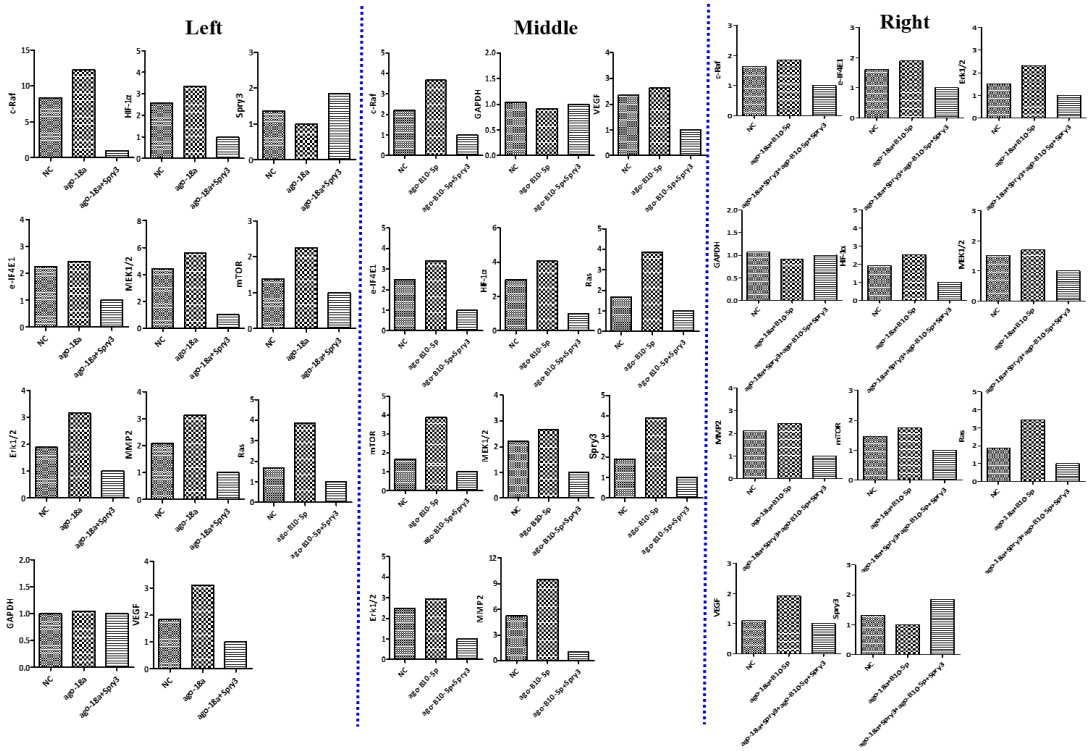

Figure S14 Quantitative analysis of western blot result by using Image J for Figure S5B .

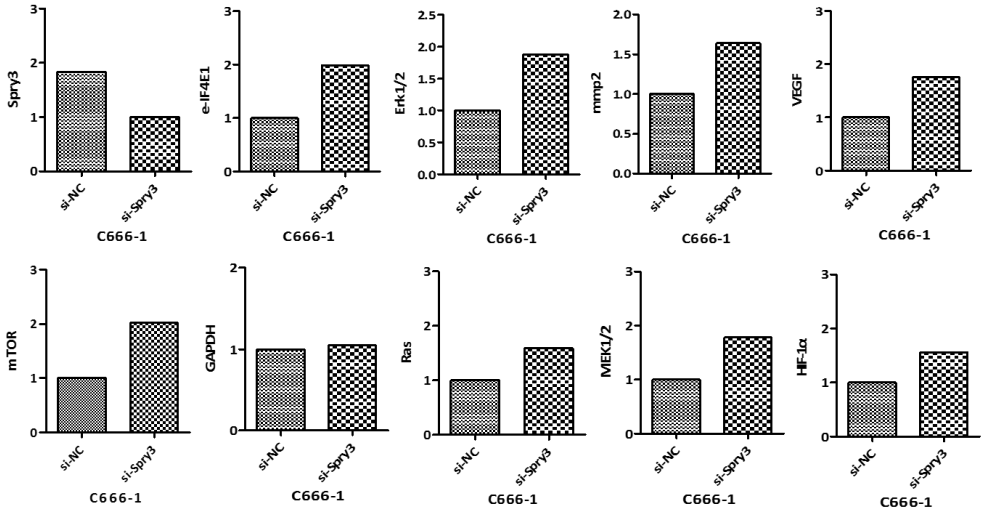

Figure S15 Quantitative analysis of western blot result by using Image J for Figure S5C .

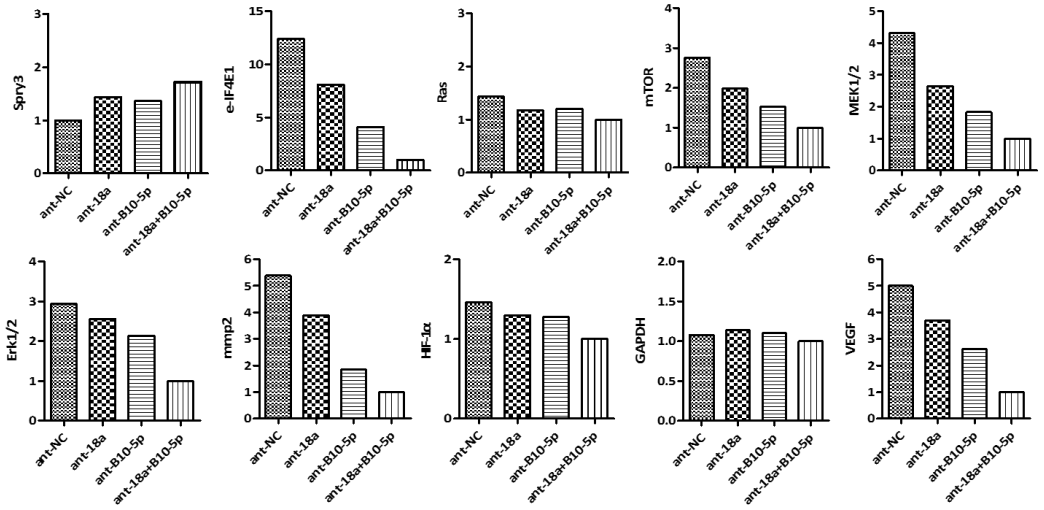

Figure S16 Quantitative analysis of western blot result by using Image J for Figure S5D .

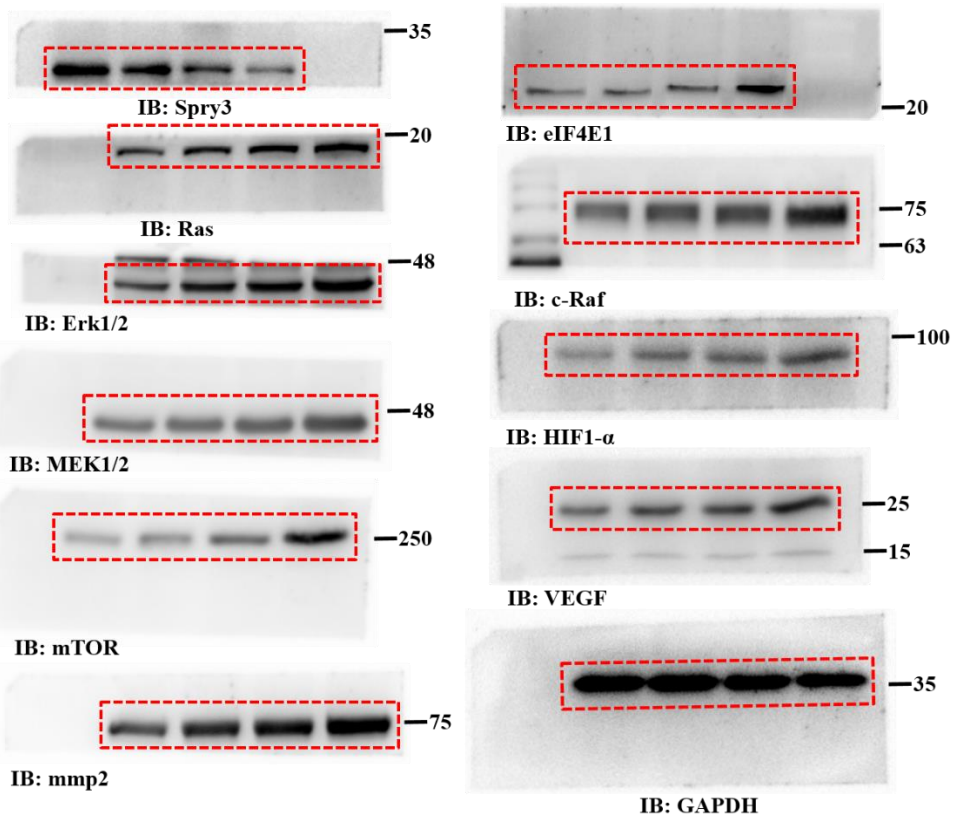

Figure S18 Original bands of western blot for Figure 3D.

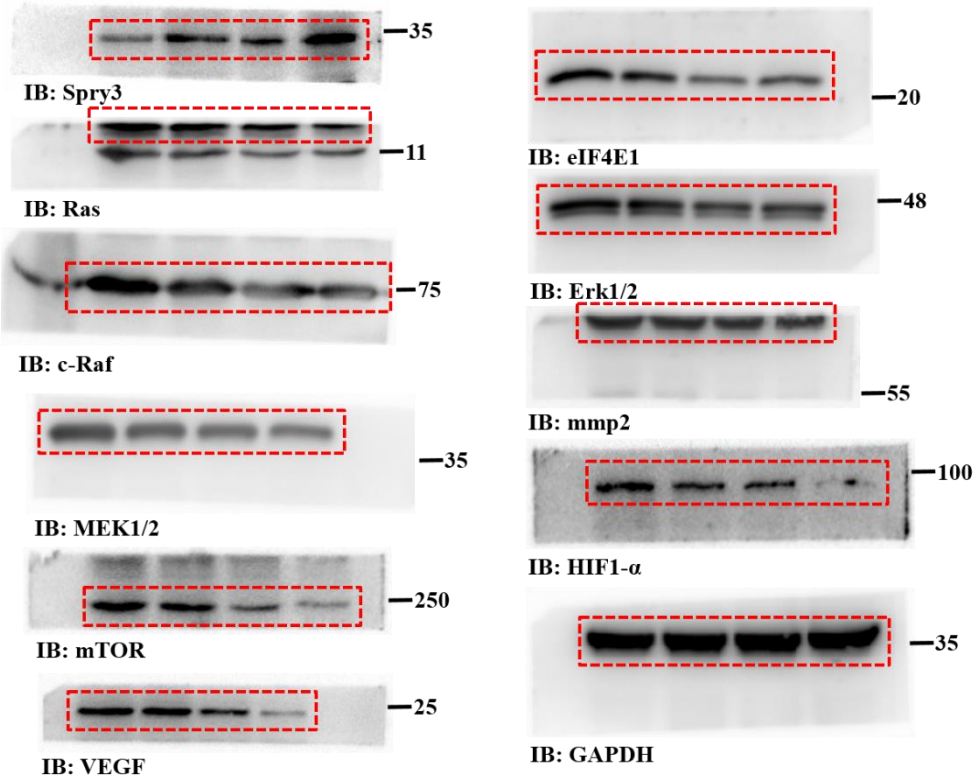

Figure S19 Original bands of western blot for Figure 3E.

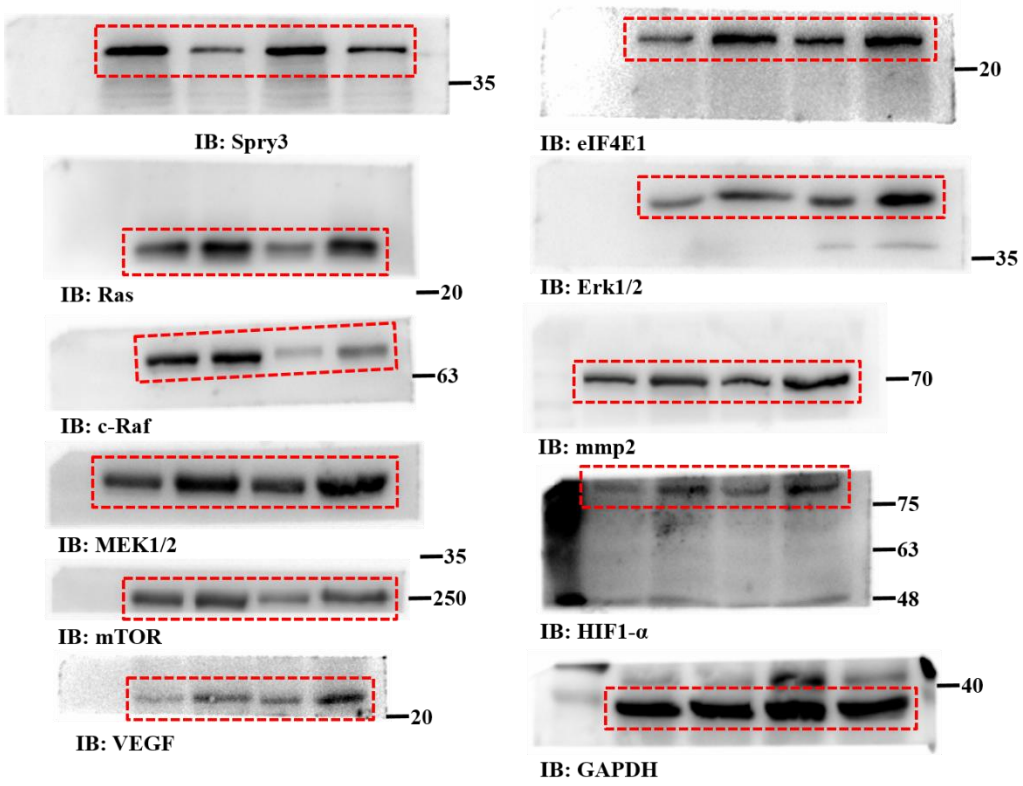

Figure S20 Original bands of western blot for Figure 3F.

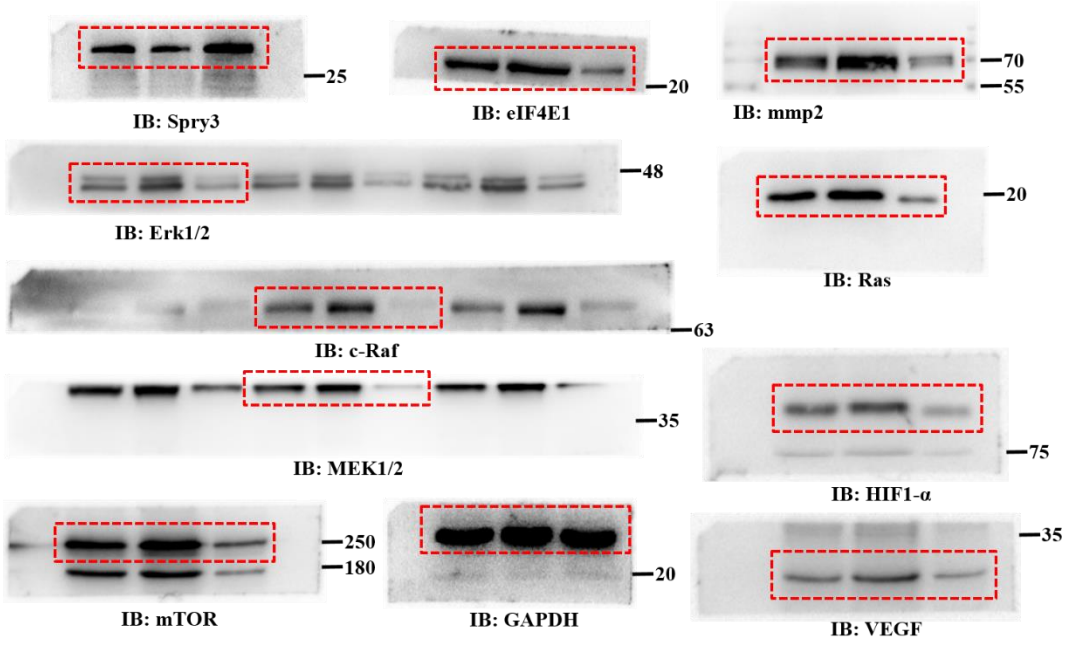

Figure S21 Original bands of western blot for Figure S5B left.

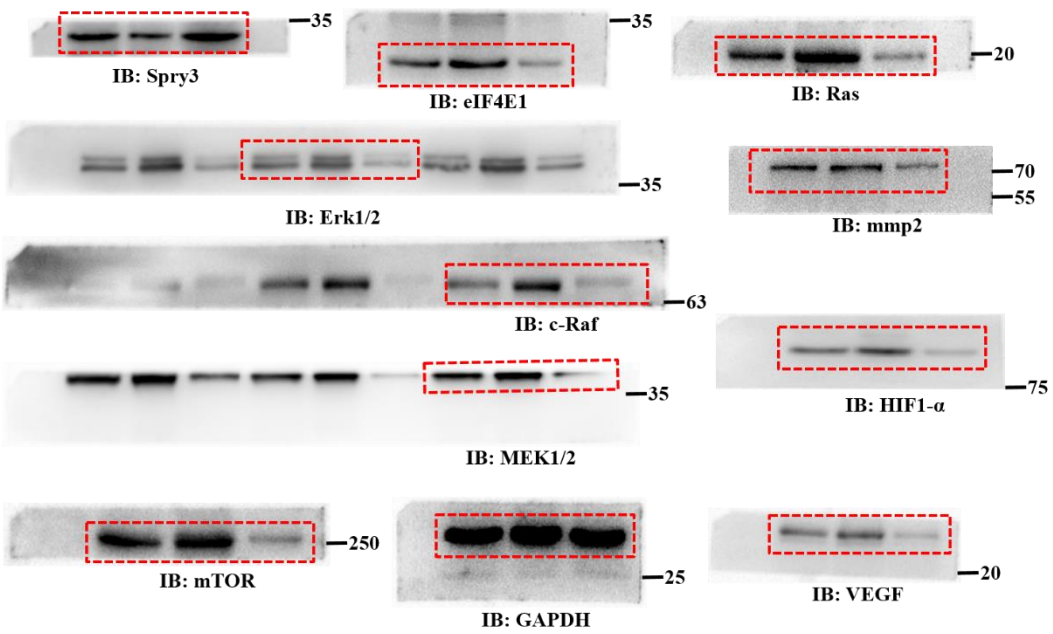

Figure S22 Original bands of western blot for Figure S5B middle.

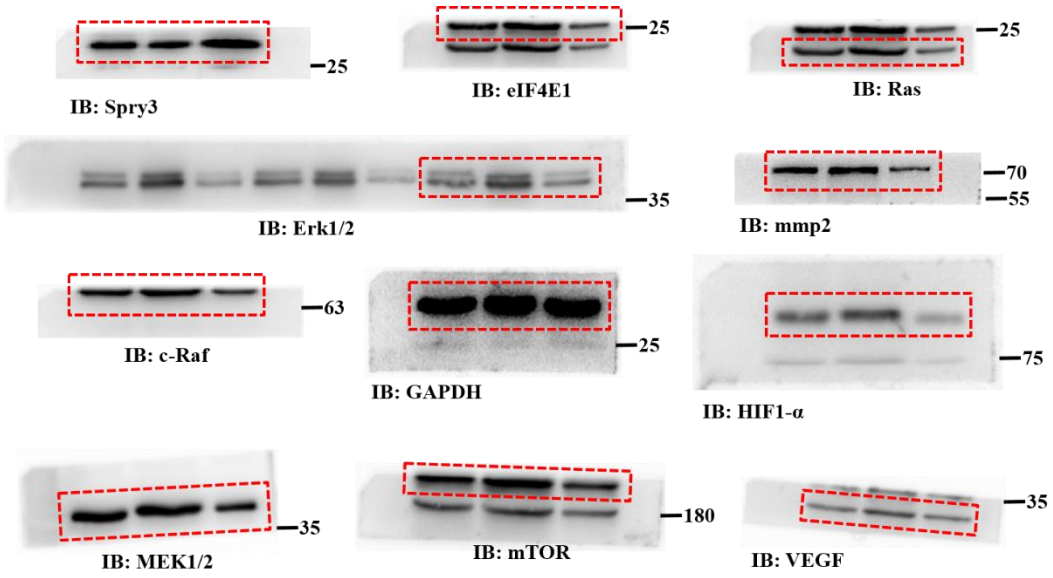

Figure S23 Original bands of western blot for Figure S5B right.

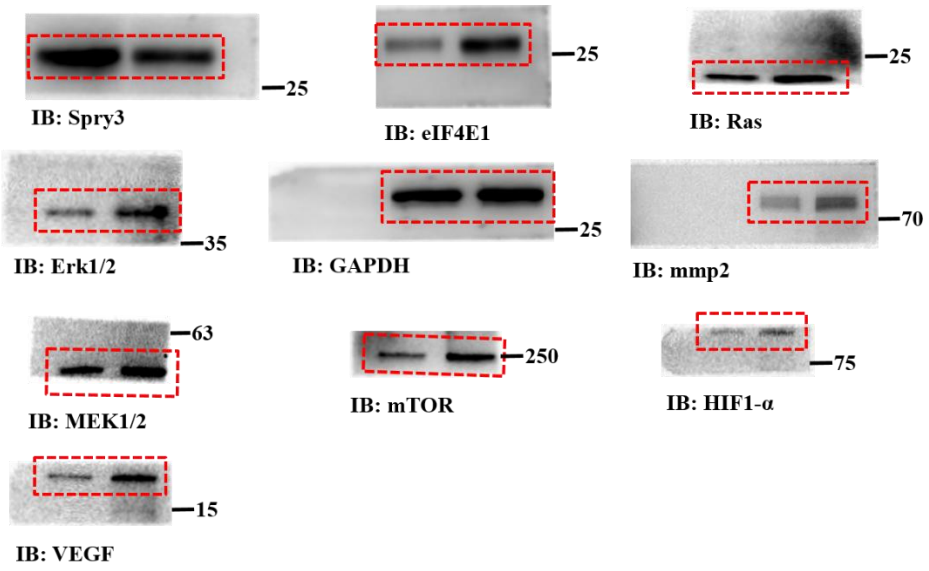

Figure S24 Original bands of western blot for Figure S5C.

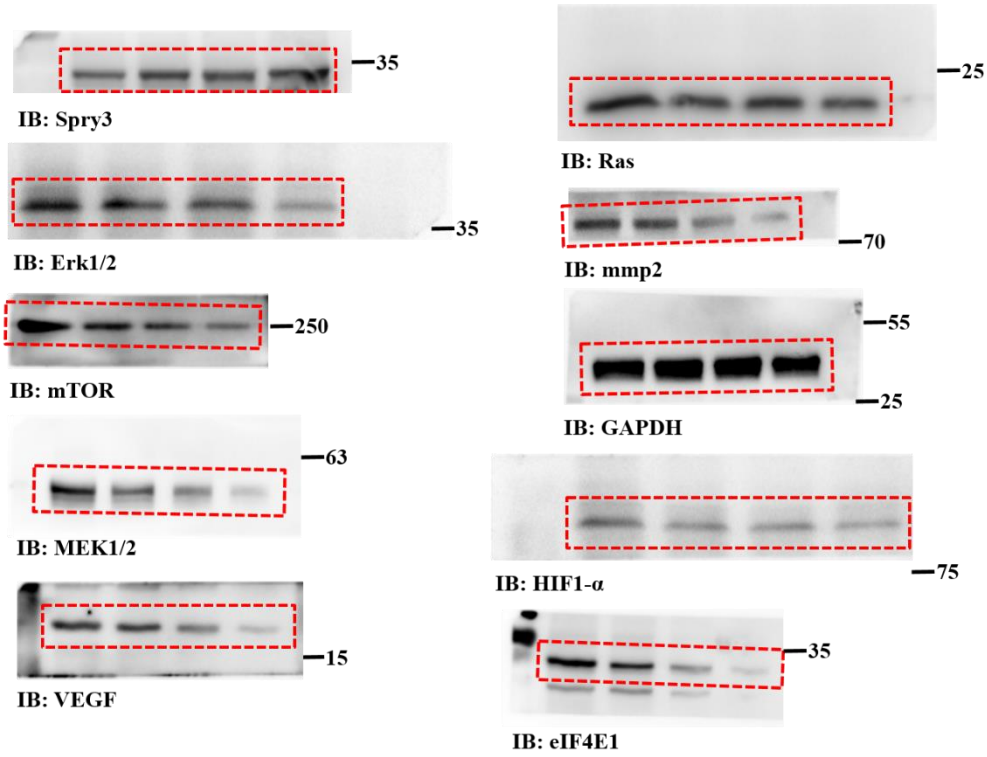

Figure S25 Original bands of western blot for Figure S5D.

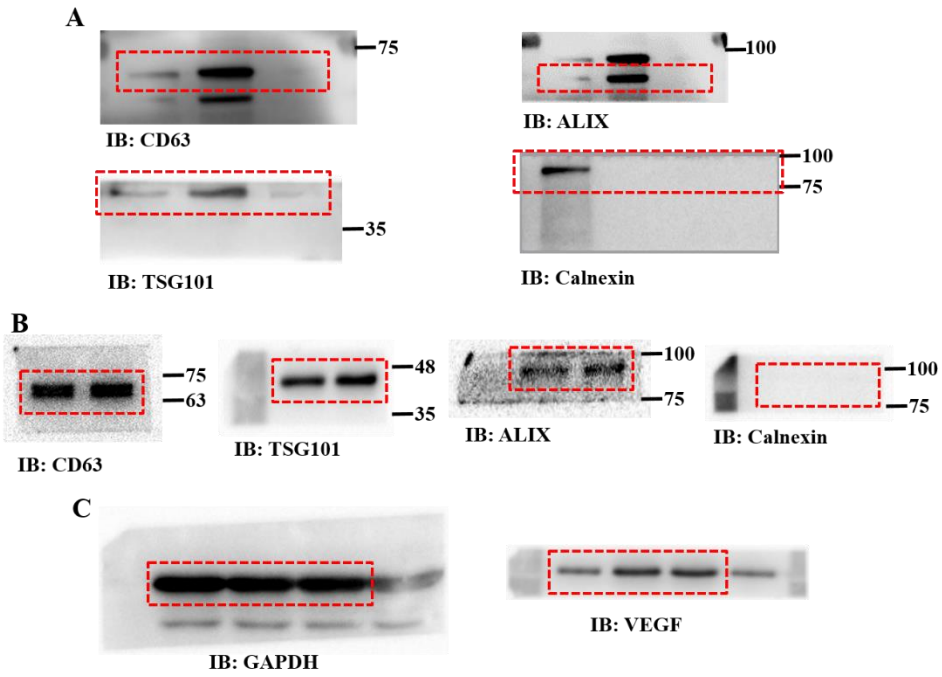

Figure S17 A) Original bands of western blot for Figure S7A, B) for Figure S10E, C) for Figure 1E.

Table S1 Antibodies and its diluted concentration involved in article.

Antibody	Brand	Cat.No	Mol weight	Dilution rate
CD63	abcam	ab134045	30-65 kDa	WB (1:1000)
TSG101	abcam	ab125011	45 kDa	WB (1:1000)
ALIX	abcam	ab186429	97, 80 kDa	WB (1:1000)
Calnexin	abcam	ab133615	90 kDa	WB (1:1000)
Spry3	abcam	ab180037	31 kDa	WB (1:1000)
Ras	abcam	ab52939	18 kDa	WB (1:10000)
c-Raf	abcam	ab181115	73 kDa	WB (1:1000)
MEK1/2	abcam	ab178876	43,44 kDa	WB (1:20000)
mTOR	abcam	ab32028	250 kDa	WB (1:1000)
eIF4E1	abcam	ab33766	30 kDa	WB (1:500)
Erk1/2	abcam	ab184699	44, 42 kDa	WB (1:10000)
HIF1-α	abcam	ab51608	93 kDa	WB (1:500)
mmp2	abcam	ab92536	74 kDa	WB (1:1000)
VEGF	abcam	ab52917	23 kDa	WB (1:1000)
GAPDH	proteintech	10494-1-AP	36 kDa	WB (1:2000)
αv	abcam	ab179475	125, 135 kDa	IHC-P (1:1000)
β3	abcam	ab210515	100 kDa	IHC-P (1:20000)